Journal of Asian Earth Sciences 130 (2016) 23–45

Contents lists available at ScienceDirect

Journal of Asian Earth Sciences

journal homepage: www.elsevier.com/locate/jseaes

The Paleozoic tectonic evolution and metallogenesis of the northern margin of East Junggar, Central Asia Orogenic Belt: Geochronological and geochemical constraints from igneous rocks of the Qiaoxiahala Fe-Cu deposit

Pei Liang [a,b], Huayong Chen [a,e,*], Pete Hollings [c], Bing Xiao [a,b], Chao Wu [a,b], Zhiwei Bao [a], Keda Cai [d]

[a] Key Laboratory of Mineralogy and Metallogeny, Guangzhou Institute of Geochemistry, Chinese Academy of Sciences, Guangzhou, Guangdong 510640, China
[b] Graduate University of Chinese Academy of Sciences, Beijing 100049, China
[c] Department of Geology, Lakehead University, Thunder Bay, Ontario P7B5E1, Canada
[d] Xinjiang Research Center for Mineral Resource, Xinjiang Institute of Ecology and Geography, Chinese Academy of Sciences, Urumqi, Xinjiang 830011, China
[e] State Key Laboratory of Ore Deposit Geochemistry, Institute of Geochemistry, Chinese Academy of Sciences, Guiyang, Guizhou 550002, China

ARTICLE INFO

Article history:
Received 29 February 2016
Received in revised form 18 July 2016
Accepted 1 August 2016
Available online 4 August 2016

Keywords:
Qiaoxiahala Fe-Cu deposit
Devonian-Carboniferous East Junggar
Central Asian Orogenic Belt
Tectonic evolution
Metallogenesis
Geochemistry

ABSTRACT

The East Junggar terrane (NW China) is an important constituent of the Central Asian Orogenic Belt (CAOB). From the Devonian to Permian, regional magmatism evolved from mainly calc-alkaline (I-type) to alkaline (A-type). The Qiaoxiahala Fe-Cu deposit, located in the Late Paleozoic Dulate island arc (northern margin of the East Junggar), is hosted in the volcanic rocks of the Middle Devonian Beitashan Formation. Two magmatic stages were identified in the deposit, the Qiaoxiahala diorite porphyry (380 ± 4.0 Ma) and a younger aplite (331 ± 3.1 Ma).

The (high-K) calc-alkaline Beitashan Formation basaltic rocks are characterized by LILE and LREE enrichments and HFSE depletions, pointing to a subduction-related affinity. The high Mg# (42–75), elevated Ce/Th and Ba/Th, depleted Nb, positive $\varepsilon_{Nd}(t)$ (6.6), low $(^{87}Sr/^{86}Sr)_i$ (0.7037) and MORB-like Pb isotope characters all suggest an origin involving partial melting of a MORB-like depleted mantle wedge (metasomatized by slab-derived fluids) with little evidence of crustal contamination.

The calc-alkaline (I-type) diorite porphyry, characterized by LILE and LREE enrichments and HFSE depletions, may have formed from fractional crystallization of the basaltic rocks, with its parental magma derived from the same depleted mantle wedge. The negative $\varepsilon_{Hf}(t)$ (−8.26), Hf model age (T^C_{DM}) of 1406 Ma and the presence of inherited zircons (ca. 470 and 506 Ma) indicate that the diorite has assimilated older crustal material.

The alkaline, metaluminous (A-type) aplite is characterized by HFSE enrichment and depletions in Sr, P and Ti, distinct from the basaltic rocks and diorite porphyry at Qiaoxiahala. The low Mg# (35–38), positive Zr and Hf, positive $\varepsilon_{Hf}(t)$ (4.77–9.75) and $\varepsilon_{Nd}(t)$ (6.85–6.86) and low T_{2DM} (538–520 Ma) suggest a juvenile lower crustal source due to partial melting of basaltic lower crust as a result of underplating of mantle-derived melts and accompanied by magma mixing.

The tectonic evolution of the Paleozoic East Junggar was associated with the initiation of subduction of the Paleo-Asian Ocean, with the formation of an island arc during the Early to Middle Devonian and generation of the coeval arc-related Fe-Cu (-Au) and porphyry Cu mineralization. Collision between the Chinese Altay and East Junggar happened in the Late Devonian with Early Carboniferous post-collisional tectonics likely explaining the synchronous Cu-Mo mineralization, while the late-Early to Late Carboniferous post-orogenic event ended without related mineralization in Qiaoxiahala.

1. Introduction

The Central Asian Orogenic Belt (CAOB), the largest Paleozoic to Mesozoic accretionary orogenic belt in the world (Sengor et al., 1993), is situated between the Siberian craton to the north and

* Corresponding author at: Key Laboratory of Mineralogy and Metallogeny, Guangzhou Institute of Geochemistry, Chinese Academy of Sciences, 511 Kehua Road, Guangzhou 510640, China.
E-mail address: huayongchen@gig.ac.cn (H. Chen).

http://dx.doi.org/10.1016/j.jseaes.2016.08.001
1367-9120/

the North China-Tarim craton to the south, and extends from the Urals in the west to the Pacific Ocean in the east (Fig. 1a). The belt is composed of numerous tectonic units, including island arcs, ophiolites, accretionary complexes, oceanic plateaus and (micro)-continental blocks (Jahn et al., 2000; Windley et al., 2002; T. Wang et al., 2006; Sun et al., 2008; Xiao et al., 2008; Huang et al., 2014). Because of the allochthonous nature of the many terranes and their complex amalgamation history, a number of models have been proposed to account for formation of the CAOB, including (1) successive accretion of the long-lived Kipchak-Tuva-Mongol subduction arc (Sengor et al., 1993); (2) accretion-collision of multiple-subduction systems, similar to the present-day SW Pacific archipelago (Coleman, 1989; Windley et al., 2002, 2007; Xiao et al., 2004, 2009) and (3) fore-arc accretion punctuated by the opening and closure of back-arc basins (Yakubchuk, 2004; Long et al., 2012).

The northern margin of the East Junggar is located in the north-central part of the Central Asian Orogenic Belt (Fig. 1a). Despite decades of research, its Early Devonian to Late Carboniferous tectono-metallogenic evolution is still far from clear, with the major debate focusing mainly on: (1) whether the Devonian tectonic setting was an island arc (Windley et al., 2002; Zhang et al., 2009), active continental margin (Chen and Jahn, 2004), rift (Wei and Ni, 1990) or mantle plume (Cai et al., 2010); (2) whether the orogenic activities between the Siberian plate (Altay terrane) and the Kazakhstan-Junggar block (Junggar terrane) were completed in the Early Carboniferous (Tong et al., 2012), Late Carboniferous (T. Wang et al., 2010) or Permian (B. Han et al., 2006; C. Han et al., 2006; Zhou et al., 2009)? (3) the relationship between the tectonic evolution and metallogenesis.

In this study, we present zircon U-Pb age and Lu-Hf isotopes, whole-rock geochemical and Sr-Nd-Pb isotopic data for the basaltic rocks, diorite porphyry and aplite from the Qiaoxiahala Fe-Cu deposit, and discuss their petrogenesis and reconstruct the regional tectonic evolution and metallogenesis.

2. Regional geology

The Junggar block, comprising the East Junggar and West Junggar terranes and the Junggar Basin, is located among the Siberian and Kazakhstan plates and the Tianshan fold belt, with the Zaisan-Erqis-Main Mongolian lineament/suture forming the northern boundary (Fig. 1b; Chen and Jahn, 2004). The East Junggar terrane comprises Devonian to Permian volcanic rocks and abundant igneous intrusions with minor sandstone, limestone lenses, chert and conglomerate. Two ophiolitic belts (namely the Armantai and Kelameili) divide the East Junggar into three tectonic units, from north to south these are the Dulate, Yemaquan arc and Harlik magmatic arcs (Fig. 1b).

The northern margin of the East Junggar terrane is located in the Late Paleozoic Dulate magmatic arc, which is separated from the southern Altay to the north by the Erqis Fault (or Irtysh Fault), one of the largest transcurrent faults in the CAOB. Exposed strata in the region comprise mainly upper Paleozoic volcano-sedimentary rocks (Fig. 1c), including (from the bottom to top) the Tuoranggekuduke Formation (D_1) marine pyroclastic and sedimentary rocks, the Beitashan Formation (D_2) mafic to intermediate volcanic, pyroclastic and carbonate rocks; the Yundukala Formation (D_2) shallow marine fine-grained clastic rocks intercalated with intermediate-mafic volcanic rocks; the Jiangzierkuduke Formation (D_3) pyroclastic rocks (dominantly tuffs), interbedded sandstone, basaltic andesite, andesite and dacite; the Nanmingshui Formation (C_1) volcano-sedimentary rocks; the Batamayineishan Formation (C_2) basalt and basaltic andesite with minor interbedded andesite, rhyolite, tuff, siltstone and carbonaceous shale and the Zhaheba Formation (P) continental coal-bearing sedimentary rocks (Zhang et al., 2009; Li et al., 2014).

Two Late Paleozoic intrusive belts are exposed in the northern margin of the East Junggar terrane, consisting dominantly of Late Paleozoic felsic intrusions (calc-alkaline granites, alkaline granites and late porphyritic dikes), with minor two-stage Paleozoic mafic-ultramafic rocks (Li and Chen, 2004). One belt is located to the northwest of the Zhaheba area and the other between the Erqis and Fuyun faults (Fig. 1c). Two magmatic peaks at ca. 390–370 Ma and ca. 330–280 Ma in the northern margin of the East Junggar have been reported by B. Han et al., (2006), C. Han et al. (2006), Wang and Xu (2006), Xue et al. (2010) and Lu et al. (2012), with evolution from mostly I-type calc-alkaline to A-type alkaline granitoids. The magmatic evolution is consistent with the regional tectonic evolution of an island arc tectonic setting from the Silurian to the Devonian, followed by the post-collisional and continental stretching event from the Carboniferous to the Permian (J. Xu et al., 2001; Y.G. Xu et al., 2001; Lu et al., 2013).

3. Ore deposit geology

The Qiaoxiahala deposit (30 km southeast of Fuyun City, Xinjiang, China) is situated on the southern margin of the Erqis Fault (Fig. 1c). The Yundukala Formation (D_2), Beitashan Formation (D_2), Nanmingshui Formation (C_1) and Quaternary sediments are exposed in the vicinity of the deposit but the deposit is primarily hosted by the Beitashan Formation (Fig. 2a).

The Beitashan Formation is exposed in the central and southwestern part of the study area (Fig. 2a), and can be divided into three members. The lower member consists of basalt, basaltic tuff, basaltic breccia, picrite and ankaramite. The ankaramite flow, located at the top of the lower member, is 5–10 m thick and interbedded with basaltic lavas. No clear boundary between the ankaramite and the basalt was observed. The picrite layer thickens to the southeast (ca. 2–100 m) and includes 8–15 flows with individual thicknesses of ca. 2–7 m. The middle member comprises aphyric basalt alternating with pyroxene-phyric basalt, basaltic andesite tuff and breccia, agglomerate and andesite, which are locally intercalated with limestone and tuffaceous siltstone. The upper member is composed of tuffaceous conglomerate, tuff, basalt, and andesite with interbedded sandstone, siltstone, marble and chert, and generally hosts the mineralization. The Yundukala (D_2) Formation conformably overlies the Beitashan Formation in the southwestern and northern parts of the deposit, and consists of tuff, tuffaceous siltstone and fine sandstone interlayered with tuffaceous conglomerate and crystal tuff. The Nanmingshui Formation (C_1) is located in the southern part of the deposit (Fig. 2a), and comprises coarse (tuffaceous) sandstones and schist intercalated with chert and limestone lenses.

Intrusive rocks are widely exposed in the central and eastern parts of Qiaoxiahala (Fig. 2b), and predominantly comprise intermediate-felsic dykes, apophyses and stocks of diorite, granodiorite, diorite porphyry and aplite. Some dykes (including aplite dykes) and stocks intrude along the NW-trending strata and regional structures, and are parallel to the mineralization belt. Diorite porphyry is the most common intrusive rocks and intrudes the Middle Devonian volcano-sedimentary rocks.

Major structures at Qiaoxiahala are mainly NW-trending (and minor NE-trending) faults (Fig. 2a). The NW-striking faults are commonly offset by the NE-striking ones which also crosscut both strata and orebodies in the deposit. The regional Erqis Fault is present as a series of NW-striking branching faults consistent with the strike of the ore bodies.

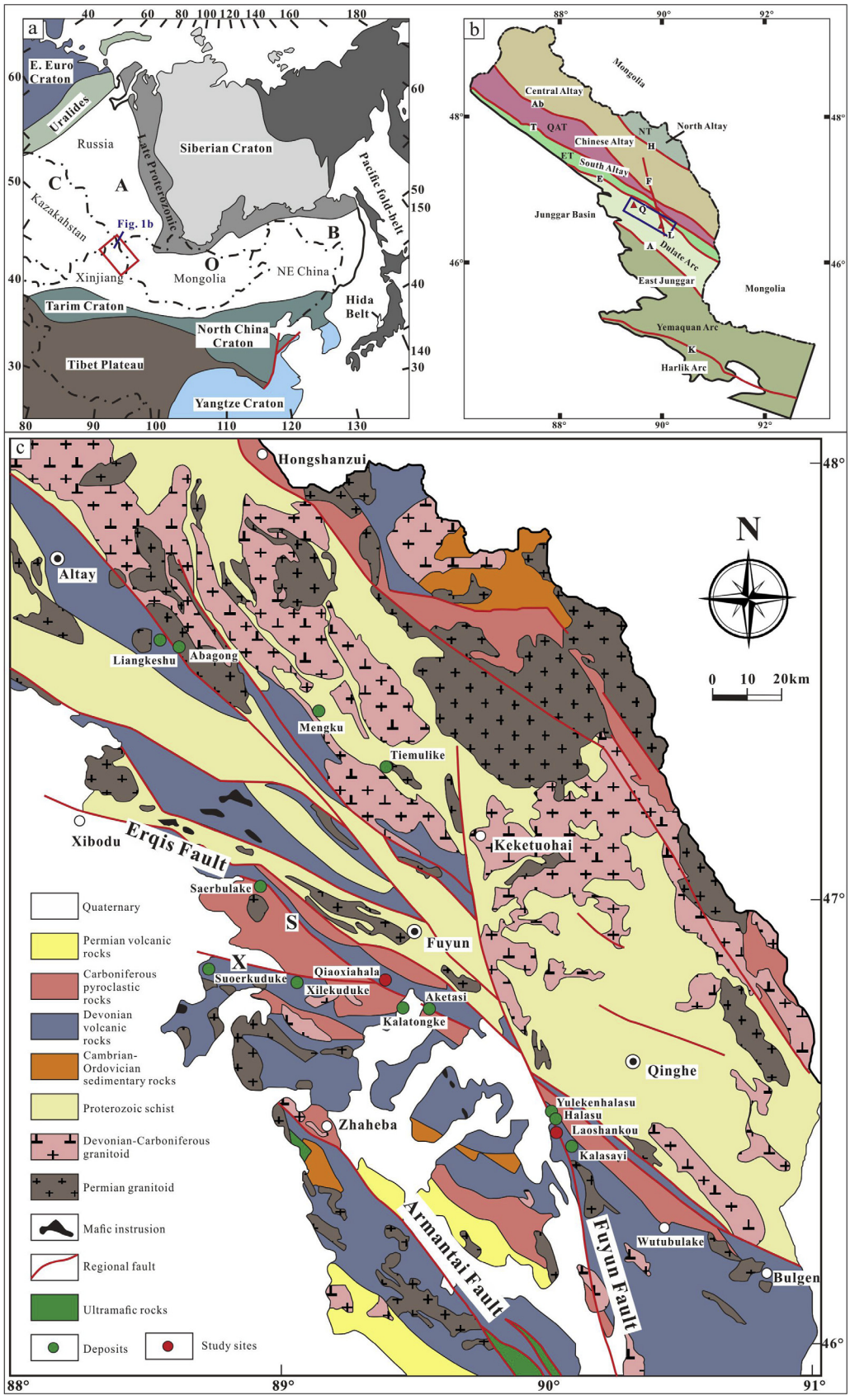

Fig. 1. (a) Simplified tectonic divisions of the Central Asian Orogenic Belt (CAOB) (modified from Chen and Jahn, 2002; Jahn et al., 2000). (b) Simplified geological map of the Chinese Altai and the East Junggar (modified from X. Long et al., 2010; Wan et al., 2011; Windley et al., 2002). (c) Regional geological and metallogenic map of the southeastern Altay orogenic belt and northeastern Junggar terrane, northern Xinjiang (modified from Li et al., 2014; Pirajno et al., 2008). Abbreviations: E. Euro Craton, East European Craton; NE China, Northeast China; H, Hongshanzui Fault; Ab, Abagong Fault; T, Tesibahan Fault; E, Erqis Fault; F, Fuyun Fault; A, Armantai Fault; K, Kelameili Fault; S, Suoerkuduke-Aketasi Fault; X, Xilekuduke-Kalatongke Fault; NT, Norte Terrane; CA, Central Altay Terrane; QAT, Qiongkuer-Abagong Terrane; ET, Erqis Terrane; L, Laoshankou deposit; Q, Qiaoxiahala deposit.

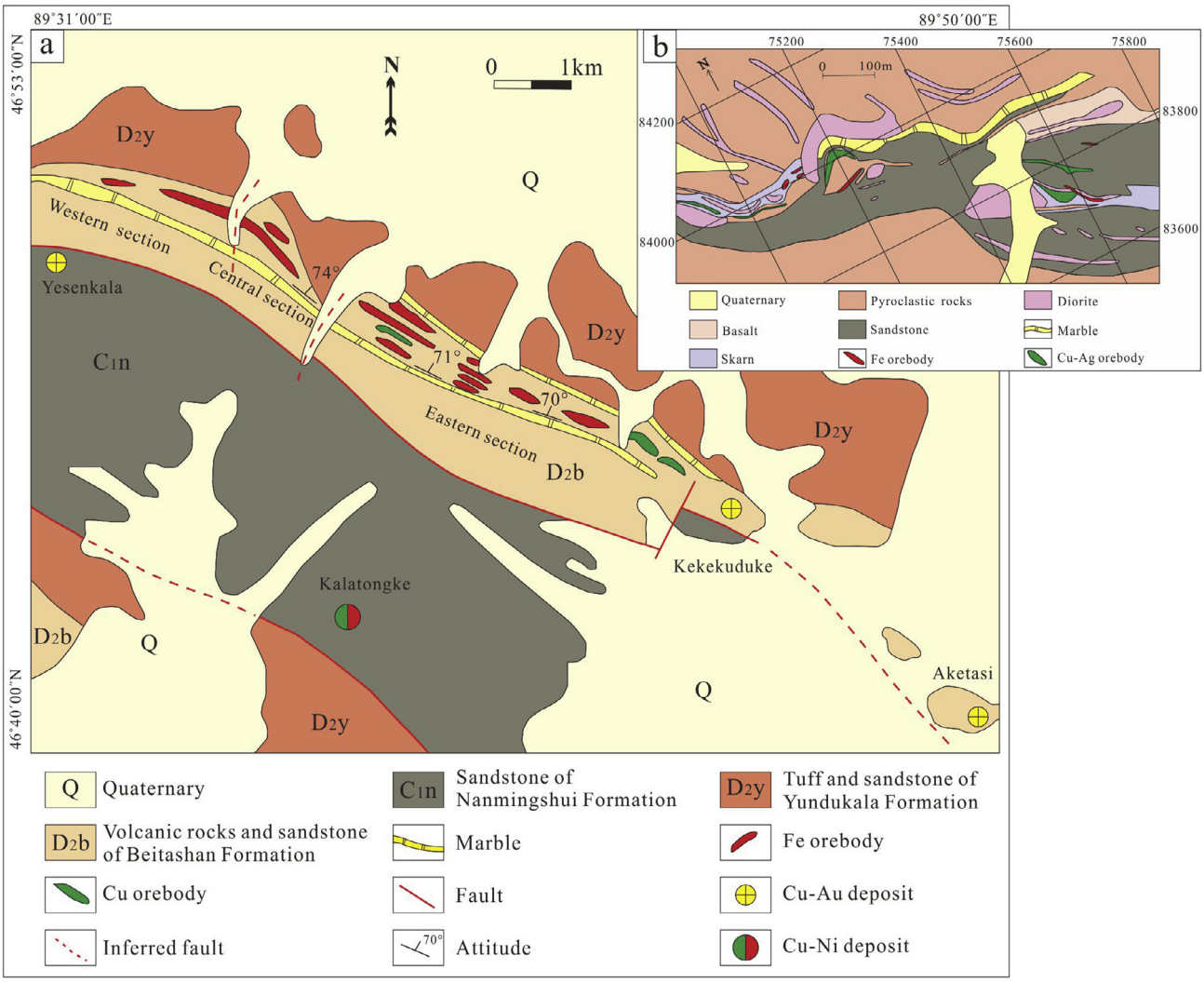

Fig. 2. (a) Geological map of Qiaoxiahala Fe-Cu-Au deposit (modified from Li et al., 2014; Yan et al., 2005; Ying, 2007). (b) Geological map of the eastern part of the Qiaoxiahala deposit (modified from Li et al., 2014; Yan et al., 2005; Ying, 2007).

4. Samples and analytical methods

Eleven least altered samples from the Qiaoxiahala deposit, including two basalts, two basaltic pyroclastic rocks, five diorite porphyries and two aplites, were selected for whole-rock major and trace element, zircon U-Pb dating and Sr-Nd-Pb-Hf isotope analyses (Table 1).

4.1. Petrographic description of samples

The basalts (green to grey in color) are porphyritic and contain phenocrysts (50–60%) dominated by hornblende (0.1–1 mm; ~40%; anhedral granular or acicular and locally chlorite altered), subordinate pyroxene (0.1–0.5 mm; ~10%; anhedral granular) and rare titanite set in a groundmass of plagioclase, hornblende and anhedral granular magnetite (Fig. 3a). The plagioclase groundmass crystallized around the hornblende phenocrysts without clear crystal forms. Late calcite veinlets occur locally.

The Beitashan Formation pyroclastic rocks include mainly breccias and tuffs. The breccia clasts (clast size: ca. 10–20 cm) have a porphyritic texture, with phenocrysts (60–80%) of pyroxene (10%; ~1 mm; euhedral and chlorite altered), plagioclase (60%), hornblende (10%) and rare titanite, in a groundmass of plagioclase, hornblende and anhedral granular magnetite (Fig. 3b). The breccia clasts are similar to the dolerites, which have high crystallinity and have been found in the Beitashan Formation at the Laoshankou deposit (Liang et al., submitted for publication). The tuffs consist of ~15% basalt and andesite lithic fragments, 25–40% crystal fragments, and ~50% volcanic ash (Fig. 3c) with moderate epidote, chlorite and carbonate alteration. The crystal fragments comprise 20% plagioclase, 15% amphibole and 5% alkali-feldspar, and rare magnetite, quartz and apatite.

The diorite porphyry (grey or red[1] in color) contains phenocrysts (40–50%) in a groundmass of plagioclase, hornblende and magnetite. The phenocrysts comprise mainly plagioclase (0.4–1 mm; 20–30%; euhedral with local carbonate alteration), hornblende (0.1–1 mm; 15–20%; anhedral-subhedral) and rare apatite and sphene with variable modal abundance and size (Fig. 3d).

The aplite (white in color) is porphyritic (Fig. 3e and f) and contains a groundmass (90%) dominated by microcrystalline feldspar (40%; mainly Na-rich plagioclase with alkali-feldspar), quartz (50%) and rare amphibole, whereas the phenocrysts comprise mainly anhedral-subhedral K-feldspar (0.01–0.04 mm; ~5%), quartz (0.01–0.04 mm; ~5%) with accessory minerals of rare zircon and apatite. Amphibole typically occurs as veins in the interstices

[1] For interpretation of color in Fig. 3, the reader is referred to the web version of this article.

Table 1
Sample locations for the Qiaoxiahala deposit.

Sample	Lithology	Localities	Analysis
QX-041	Basalt	46° 48′ 51.58″ N; 89° 39′ 15.84″ E	Major and trace element
QX-052	Basalt	46° 48′ 23.72″ N; 89° 39′ 57.25″ E	Major and trace element Sr–Nd–Pb isotope analysis
QX-039	Basaltic breccia	46° 48′ 51.58″ N; 89° 39′ 15.84″ E	Major and trace element
QX-046	Basaltic tuff	46° 48′ 28.95″ N; 89° 40′ 0.64″ E	Major and trace element
QX-036	Diorite porphyry	46° 48′ 55.61″ N; 89° 39′ 15.7″ E	Major and trace element
QX-042	Diorite porphyry	46° 48′ 51.58″ N; 89° 39′ 15.84″ E	Major and trace element
QX-043	Diorite porphyry	46° 48′ 51.58″ N; 89° 39′ 15.84″ E	Major and trace element Sr–Nd–Pb isotope analysis Zircon U–Pb geochronology Zircon Lu–Hf isotope analysis
QX-045	Diorite porphyry	46° 48′ 28.95″ N; 89° 40′ 0.64″ E	Major and trace element Sr–Nd–Pb isotope analysis
QX-058	Diorite porphyry	46° 48′ 17.43″ N; 89° 40′ 12.76″ E	Major and trace element Sr–Nd–Pb isotope analysis
QX-055-1	Aplite	46° 48′ 20.51″ N; 89° 39′ 48.45″ E	Major and trace element Sr–Nd isotope analysis Zircon U–Pb geochronology Zircon Lu–Hf isotope analysis
QX-055-2	Aplite	46° 48′ 20.51″ N; 89° 39′ 48.45″ E	Major and trace element Sr–Nd isotope analysis

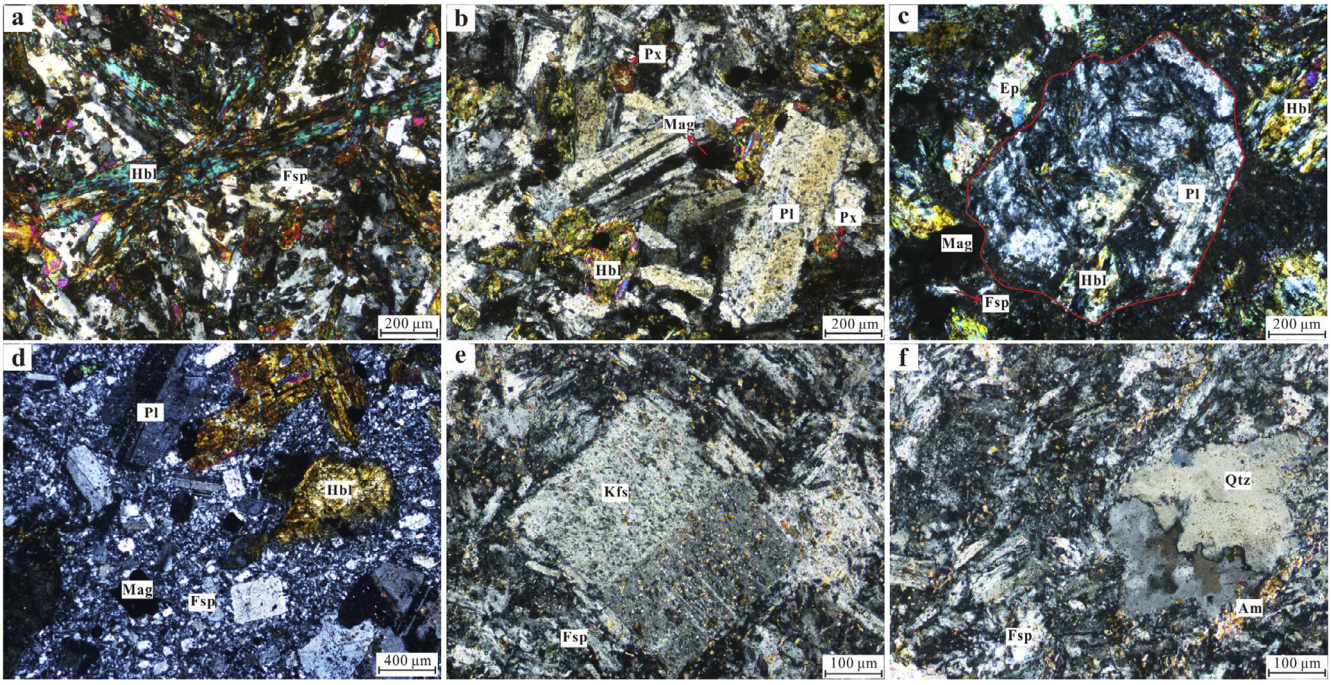

Fig. 3. Photomicrographs of the main facies types under cross-polarized light for samples from the Qiaoxiahala deposit. (a) hornblende phenocrysts in plagioclase groundmass (Beitashan Formation basalt QX-052); (b) hornblende, pyroxene and plagioclase phenocrysts (Beitashan Formation doleritic volcanic breccia QX-039); (c) basalt fragments in the basaltic tuff (QX-046); (d) hornblende and plagioclase phenocrysts in feldspar groundmass (diorite porphyry QX-042); (e) and (f) feldspar and quartz phenocrysts in a groundmass of quartz, feldspar and muscovite (aplite QX-055-1). Abbreviations: Am – amphibole; Ep – epidote; Fsp – feldspar; Hbl – hornblende; Kfs – K-feldspar; Pl – plagioclase; Px – pyroxene; Qtz – quartz; Mag – magnetite.

between the feldspar and quartz. Moderate silicic alteration is present.

4.2. Analytical methods

4.2.1. Whole-rock major and trace element analysis

Eleven whole-rock samples were milled to about 200 mesh with an agate mill. Major element contents were measured by X-ray fluorescence spectrometry (XRF) on fused glass beads using a Rigaku 100e spectrometer at the State Key Laboratory of Isotope Geochemistry, Guangzhou Institute of Geochemistry, Chinese Academy of Sciences (GIGCAS). The precision for major elements was better than 1%. Details of the XRF procedures are described by Li et al. (2005). The trace element contents were measured by a Finnigan MAT ELEMENT magnetic sector ICP-MS with the precision better than 10% at the Institute of Geochemistry, the Chinese Academy of Sciences (IGCAS). The details of the analytical procedure are outlined in Qi et al. (2000). The international standard AMH-1 (Mount Hood andesite; Thompson et al., 1999) was used as the standard for quality control. The loss on ignition (LOI) was determined after heating the samples to 1000 °C for 3 h.

4.2.2. Sr-Nd-Pb isotopic analysis

Six samples from the Qiaoxiahala deposit were selected for radiogenic isotopic analysis. Strontium-Nd-Pb isotopic compositions were measured on a Micromass IsoProbe Multi-Collector ICP-MS at the State Key Laboratory of Isotope Geochemistry, GIGCAS. For the Sr-Nd isotopic analysis, ca. 50 mg of whole-rock powder was dissolved in distilled HF-HNO_3 at 150 °C for five days in Savillex screw top Teflon beakers. After complete dissolution, the samples were dried down and dissolved in 2.5 N HCl. Strontium and rare earth elements (REEs) were separated using resin exchange columns made by the Eichrom Company with 2.5 N HCl for Sr and 6 N HCl for REEs. Neodymium was separated from the REEs using HDEHP columns with a 0.18 N HCl eluant. The measured Sr and Nd isotopic ratios were normalized to $^{86}Sr/^{88}Sr = 0.1194$ and $^{146}Nd/^{144}Nd = 0.7219$, respectively. The reproducibility of $^{87}Sr/^{86}Sr$ and $^{143}Nd/^{144}Nd$ during measurement was checked by analysis of the standards NBS987 Sr and Shin Etou with Nd yielding average values of 0.710243 ± 14 (2σ) and 0.512124 ± 11 (2σ), respectively. Total procedural blanks were 0.5 ng for Sr and 0.3 ng for Nd. Separation and purification of Pb were carried out in Teflon columns with a 100 μL (separation) and 40 μL bed (cleaning) of Bio-Rad AG1-X8 (100–200 mesh) anion exchange resin using HBr-HCl ion exchange. Lead was loaded with a Si gel onto a pre-conditioned Re filament and measured in a single filament mode. A factor of 1‰ per atomic mass unit was applied for correction of instrumental mass bias using NBS SRM 981 as reference material. Total procedural blanks for Pb were between 20 and 40 pg. Sample reproducibility is estimated at ±0.02, ±0.015 and ±0.03 (2σ) for the $^{206}Pb/^{204}Pb$, $^{207}Pb/^{204}Pb$ and $^{208}Pb/^{204}Pb$ ratios, respectively. The detailed analytical techniques are described by Wei et al. (2002) and Liang et al. (2003).

4.2.3. Zircon U-Pb geochronology

Diorite porphyry (QX-043) and aplite (QX-055-1) samples (about 1 kg each) were collected from outcrops of the Qiaoxiahala deposit for LA-ICP-MS zircon U-Pb and Hf analysis.

Prior to the analysis, zircons were separated through conventional magnetic and density separation techniques, followed by hand-picking under a binocular microscope. Zircons were selected and mounted on epoxy resin and then polished to expose the crystal center. Transmitted light microscopy and cathodoluminescence (CL) imaging were carried out to study the zircon morphology and internal structures. The CL images were obtained using a JXA-8100 Electron Probe Micro-analyzer (EPMA) with a Mono CL3 Cathodoluminescence System at GIGCAS.

Zircon U-Pb dating and *in-situ* trace element analyses were performed with an Agilent 7500a ICP-MS coupled with a Resonetics RESOlution M-50 (193 nm ArF excimer) laser ablation system (LA) at the State Key Laboratory of Isotope Geochemistry, GIGCAS. Sample mounts were placed in a specially-designed double volume sample cell flushed with Ar and He. Laser ablation was undertaken at a constant energy (81 mJ/cm^{-2}) at 10 Hz repetition rate and 31 μm spot diameter. The ablated material was carried by He-Ar gas via a Squid system to homogenize the signal to the ICP-MS. Each analysis incorporated a background acquisition time of approximately 20–30 s (gas blank) followed by 50 s of data acquisition during the ablation. Detailed analytical procedures followed those described by Liu et al. (2010). Off-line selection and integration of background and analyzed signals, and time-drift correction and quantitative calibration for trace element analyses and U-Pb dating were performed using an in-house program ICPMSDataCal 8.3 (Liu et al., 2010). The zircon standard Temora was used as an external calibration and a Qinghu standard was used as an internal calibration during U-Pb dating. Time-dependent U-Th-Pb isotopic ratio drifts were corrected using a linear interpolation every five analyses and were monitored using variations in analysis of Temora. The obtained mean $^{206}Pb/^{238}U$ ages of Temora and Qinghu are within experimental error of their recommended values (Jackson et al., 2004). The absolute abundances of U, Th and REEs were determined using an external standard glass NIST SRM 610, and ^{29}Si was used as the internal standard. Common Pb correction and ages of the samples were calculated using ComPbCorr#3_17 (Andersen, 2002). Concordia diagrams and weighted mean calculations were made using Isoplot/Ex_ver3.0 (Ludwig, 2003). $^{206}Pb/^{238}U$ ages were adopted in this study because the relative small amount of accumulated ^{207}Pb does not permit precise $^{207}Pb/^{206}Pb$ dating (Black et al., 2003).

4.2.4. Zircon Lu-Hf isotope analysis

In-situ Hf isotope analyses were performed using a Neptune Plus MC-ICP-MS (Thermo Fisher Scientific, Germany) in combination with a Resonetics RESOlution M-50 (193 nm ArF excimer) laser ablation system (LA) at the State Key Laboratory of Isotope Geochemistry, GIGCAS. The zircon analyses were conducted with a single-spot ablation mode, and with 44 μm beam diameter, 10 Hz repetition rate and 100 mJ/cm^{-2} energy. Helium was used as the carrier gas in the ablation cell and was mixed with argon (makeup gas) downstream of the ablation cell. In order to evaluate the analytical data reliability, the zircon standard Penglai (Li et al., 2008) was used for external standardization, and yielded a weighted mean $^{176}Hf/^{177}Hf$ ratio of 0.082906 ± 50 (σ). Each measurement consisted of 20 s of acquisition of the background signal acquisition followed by 50 s of ablation signal acquisition. Data were normalized to $^{179}Hf/^{177}Hf = 0.7325$, using an exponential correction for mass bias (Segal et al., 2003). The ^{176}Lu decay constant of 1.865×10^{-11} yr^{-1} (Scherer et al., 2001) was used to calculate the initial $^{176}Hf/^{177}Hf$ ratios. The chondritic values of $^{176}Hf/^{177}Hf = 0.0332$ and $^{176}Lu/^{177}Hf = 0.282772$ reported by Blichert-Toft and Albarède (1997) were used for calculating $\varepsilon_{Hf}(t)$ values. The depleted mantle Hf model ages (T_{DM}) were calculated using the measured zircon $^{176}Lu/^{177}Hf$ ratios, based on the assumption that the depleted mantle reservoir has a linear isotopic growth from $^{176}Hf/^{177}Hf = 0.279718$ (at 4.55 Ga) to 0.283250 (at present), with $^{176}Lu/^{177}Hf = 0.0384$ (Griffin et al., 2000). The T_{DM} model age can only give a minimum age for the source material of the magma from which the zircon crystallized, because fractionation between Lu and Hf occurs when zircons are formed. Therefore, the Hf model age T_{DM}^{C} was calculated, which is derived from projecting the initial $^{176}Hf/^{177}Hf$ of a zircon (after determination of its U/Pb age) back to the depleted mantle model growth line by using a $^{176}Lu/^{177}Hf$ ratio of 0.008, the mean value for the upper continental crust (Rudnick and Gao, 2003).

5. Results

5.1. Whole-rock geochemistry

5.1.1. Volcanic rocks

The Devonian volcanic rocks at Qiaoxiahala are mainly basaltic with SiO_2 of 45.15–52.23 wt.%, high Na_2O (1.93–5.70 wt.%) and low K_2O (0.34–5.47 wt.%) with total ($Na_2O + K_2O$) = 4.00–9.70 wt.% and Na_2O/K_2O = 0.75–14.59. Al_2O_3 contents of 11.68–20.00 wt.%, A/CNK (mole $Al_2O_3/[CaO + Na_2O + K_2O]$) ratios of 0.35–0.86 and A/NK (molar $Al_2O_3/[Na_2O + K_2O]$) ratios of 1.22–2.64. The basaltic rocks show a wide range of FeO^T ($Fe_2O_3^T$*0.8998; 7.07–12.32 wt.%) and MgO (2.80–8.34 wt.%) with Mg# (Mg/[Mg + Fe]*100) = 42–65. The TiO_2 content is mostly below 1 wt.% but range from 0.57 to 1.53 wt.% (Table 2).

The total REE (∑REE) content of the basaltic rocks varies from 46.9 to 98.3 ppm (mean 68.2 ppm). LREE/HREE ratios range from 2.58 to 8.24, mean 4.57 ($(La/Sm)_N$ = 1.09–2.27, mean 1.84;

Table 2
Whole-rock geochemistry of volcanic and intrusive rocks from the Qiaoxiahala deposit.

Sample:	QX-041	QX-052	QXH31	QXH34	QXH36	QXH46	QXH47	QXH79	QXH81	QXH109	QXH111	QXH112	QXH113	QX-039	QX-046	QX-036	QX-058	QX-042	QX-043	QX-045	QX-055-1	QX-055-2
Lithology	Basalt													Basaltic pyroclastic rock		Diorite porphyry					Aplite	
SiO_2	52.23	50.04	45.90	45.69	45.15	51.47	51.42	47.09	47.88	49.72	48.25	49.74	50.01	51.07	47.85	54.65	57.16	58.55	58.33	60.83	80.55	83.02
TiO_2	1.07	1.19	1.01	0.57	0.72	0.60	0.64	0.67	0.80	0.84	0.95	0.80	0.76	0.81	1.53	0.49	0.59	0.48	0.49	0.33	0.08	0.08
Al_2O_3	15.37	17.45	15.49	20.00	11.68	18.04	18.03	13.14	12.87	14.85	16.82	17.26	13.92	15.67	15.37	16.84	15.91	16.34	16.27	17.25	9.99	8.48
Fe_2O_{3T}	7.86	8.61	10.75	9.15	11.89	9.13	9.54	11.36	13.69	11.24	10.23	9.61	11.55	10.88	11.63	7.06	8.34	6.97	7.09	4.87	0.80	0.73
MnO	0.13	0.13	0.16	0.20	0.22	0.20	0.21	0.20	0.24	0.23	0.19	0.14	0.18	0.13	0.19	0.10	0.12	0.10	0.10	0.10	0.07	0.06
MgO	6.02	5.22	8.39	2.80	6.75	3.67	3.97	8.04	6.25	5.41	4.88	3.57	5.79	5.60	5.48	2.92	3.14	2.58	2.65	1.50	0.21	0.17
CaO	6.94	7.41	5.18	12.95	14.83	6.27	5.31	9.80	11.30	11.08	9.37	11.94	10.52	2.94	10.39	3.49	5.07	4.69	4.42	5.44	1.19	1.09
Na_2O	3.60	3.59	4.96	3.14	2.48	5.54	5.70	3.05	1.93	3.27	3.34	3.56	2.67	4.23	3.26	4.69	4.71	4.32	4.46	4.38	3.87	3.47
K_2O	3.96	2.69	0.34	2.22	1.79	2.57	2.79	1.94	2.56	1.18	2.17	0.84	2.20	5.47	0.74	4.78	3.15	3.40	3.81	2.78	2.13	1.90
P_2O_5	0.42	0.41	0.38	0.46	0.45	0.56	0.61	0.37	0.61	0.35	0.39	0.29	0.47	0.53	0.22	0.43	0.38	0.37	0.37	0.23	0.02	0.02
LOI	1.58	2.78	7.13	2.26	4.40	1.28	1.46	4.62	2.14	2.02	3.12	2.10	1.78	1.73	2.76	3.71	1.15	1.64	1.17	1.45	0.92	0.80
Total	99.47	99.73	99.70	99.46	100.37	99.34	99.68	100.28	100.28	100.17	99.71	99.84	99.84	99.47	99.52	99.31	99.89	99.62	99.35	99.36	99.84	99.81
Mg#	64	59	65	42	57	48	49	62	52	53	53	46	54	55	52	49	47	46	47	42	38	35
Sc	19.1	24.1	43.2	18.7	43.2	18.6	20.2	43.3	38.2	38.2	36.4	28.1	33.9	26.8	36.6	14.4	21.1	15.8	16.0	7.20	3.34	2.77
Ti	6390	7180	6054	3417	4316	3596	3836	4016	4795	5035	5694	4795	4555	4780	9360	3120	3760	3140	3140	2080	492	454
V	196	241	305	403	374	241	249	336	404	306	283	252	315	227	348	152	201	152	155	82.0	5.41	4.65
Cr	173	72.0	299	12.7	98.2	5.37	6.71	144	39.2	129	56.9	43.4	116	36.0	72.0	28.0	38.0	39.0	38.0	41.0	33.6	30.1
Co	28.1	26.3	39.9	24.7	34.9	24.9	27.7	34.6	29.6	23.1	21.1	18.7	26.9	24.6	27.9	14.6	18.5	15.4	16.0	7.60	0.41	0.44
Ni	92.6	20.9	74.4	9.85	42.8	6.16	8.51	47.9	19.6	33.9	20.4	15.4	36.9	26.6	32.6	9.90	11.8	10.7	10.8	5.30	2.05	0.45
Ga	18.7	19.8	19.2	34.5	16.6	15.7	14.6	16.5	18.5	16.3	16.8	19.3	16.3	11.6	20.4	19.2	19.0	18.9	18.5	18.8	16.5	15.4
Rb	21.8	18.1	4.29	26.3	17.4	38.3	51.2	20.1	33.3	17.1	43.4	10.5	32.9	74.7	11.4	107	39.2	45.3	43.5	36.1	28.5	25.6
Sr	991	1050	311	2533	622	870	527	366	928	503	407	849	553	399	488	351	613	738	643	786	93.3	86.4
Y	13.1	18.3	16.4	13.8	16.1	16.6	17.3	16.9	23.2	20.4	19.4	19.9	18.1	18.0	26.2	15.8	20.2	16.3	16.7	14.1	17.1	15.7
Zr	62.0	85.7	70.7	42.4	45.9	50.0	53.6	50.9	52.0	59.9	65.9	63.7	56.2	43.5	34.7	68.4	79.0	77.5	75.8	65.1	92.1	86.0
Nb	4.90	5.80	3.91	2.29	1.94	2.67	2.88	2.13	2.55	2.99	3.24	3.09	2.84	2.60	2.80	3.90	3.40	5.20	5.20	5.20	18.3	18.0
Ba	1250	640	107	330	292	339	375	354	273	236	251	246	605	3600	220	1160	960	990	1060	1040	372	360
La	14.8	15.4	11.8	7.37	9.22	9.74	10.10	9.87	11.50	8.68	7.28	9.81	10.9	12.9	6.7	11.0	13.8	15.1	15.6	11.5	15.9	14.4
Ce	34.8	36.9	27.3	15.1	19.4	19.4	20.5	21.0	26.1	19.4	14.9	19.1	22.2	28.1	18.7	25.0	29.6	30.4	32.1	24.6	28.0	26.1
Pr	4.55	4.84	4.04	2.19	2.89	2.79	2.97	3.14	3.96	2.92	2.06	2.82	3.24	3.66	2.58	3.17	3.81	3.59	3.81	2.92	3.19	2.86
Nd	19.6	21.0	17.9	9.78	13.2	12.6	13.1	13.8	17.7	12.9	9.45	12.6	13.9	15.9	12.7	13.4	15.8	14.5	15.4	11.6	11.5	10.4
Sm	4.20	4.88	4.31	2.55	3.42	3.16	3.42	3.75	4.89	3.28	2.57	3.11	3.44	4.07	3.97	3.21	3.85	3.28	3.41	2.59	2.14	2.09
Eu	1.25	1.56	1.39	0.86	1.14	1.06	1.14	1.26	1.46	0.99	0.88	1.03	1.09	0.95	1.43	1.02	1.13	0.97	0.99	0.79	0.54	0.44
Gd	3.38	4.38	3.89	2.60	3.56	3.15	3.41	3.66	4.94	3.59	2.87	3.29	3.45	4.14	4.80	3.19	3.90	3.03	3.06	2.46	2.26	1.88
Tb	0.46	0.65	0.60	0.41	0.54	0.51	0.56	0.55	0.77	0.57	0.51	0.54	0.53	0.62	0.82	0.50	0.62	0.47	0.48	0.39	0.34	0.36
Dy	2.61	3.68	3.31	2.46	3.11	3.01	3.21	3.25	4.54	3.58	3.36	3.35	3.21	3.61	5.14	3.01	3.76	2.87	2.94	2.41	2.03	2.02
Ho	0.49	0.73	0.66	0.50	0.61	0.63	0.65	0.64	0.85	0.72	0.70	0.67	0.64	0.73	1.05	0.63	0.81	0.60	0.61	0.52	0.44	0.44
Er	1.32	2.06	1.75	1.37	1.61	1.76	1.81	1.72	2.28	1.98	1.96	1.89	1.76	2.03	3.01	1.87	2.45	1.82	1.83	1.60	1.46	1.28
Tm	0.16	0.27	0.25	0.20	0.23	0.27	0.27	0.25	0.33	0.30	0.31	0.29	0.27	0.28	0.40	0.28	0.35	0.26	0.26	0.24	0.24	0.22
Yb	1.03	1.70	1.63	1.28	1.39	1.68	1.75	1.49	2.01	1.92	2.01	1.81	1.64	1.80	2.29	1.85	2.26	1.74	1.74	1.61	1.56	1.44
Lu	0.16	0.26	0.24	0.20	0.21	0.26	0.27	0.22	0.29	0.29	0.30	0.27	0.24	0.30	0.33	0.30	0.36	0.29	0.28	0.27	0.26	0.24
Hf	2.00	2.30	2.13	1.26	1.58	1.52	1.64	1.64	1.77	1.86	1.96	1.88	1.74	1.40	1.30	1.90	2.30	2.20	2.20	1.90	2.45	2.43
Ta	0.28	0.31	0.22	0.13	0.11	0.16	0.17	0.12	0.14	0.17	0.20	0.18	0.17	0.16	0.20	0.24	0.21	0.35	0.34	0.33	1.19	1.05
Pb	4.30	4.60	5.47	12.2	6.52	7.78	3.85	5.23	4.74	2.70	2.12	3.44	3.74	1.60	3.00	2.70	3.60	2.70	2.50	2.60	37.2	33.3
Th	1.00	1.40	0.87	0.69	0.71	0.93	0.97	0.89	0.75	0.94	0.76	1.07	1.28	1.50	0.40	1.50	2.10	2.20	2.20	1.80	4.28	4.28
U	0.50	0.50	0.42	0.57	0.52	0.53	0.53	0.57	0.42	1.08	0.58	0.87	0.62	0.70	0.30	0.70	0.80	0.70	0.80	0.60	1.21	1.17
K	33,500	22,300	2823	18,429	14,860	21,335	23,161	16,105	21,252	9796	18,014	6973	18,263	46,400	6600	41,600	27,600	30,000	33,200	23,000	17,718	15,753
P	1940	1890	1658	2007	1964	2444	2662	1615	2662	1527	1702	1266	2051	2460	990	1990	1790	1760	1750	1020	66.0	69.6
δEu	0.98	1.01	1.02	1.01	0.99	1.02	1.01	1.03	0.90	0.88	0.99	0.98	0.96	0.70	1.00	0.96	0.88	0.92	0.92	0.94	0.74	0.66
References	①	①	②	②	②	②	②	②	②	②	②	②	②	①	①	①	①	①	①	①	①	①

① This study; ② Chai et al., 2012.

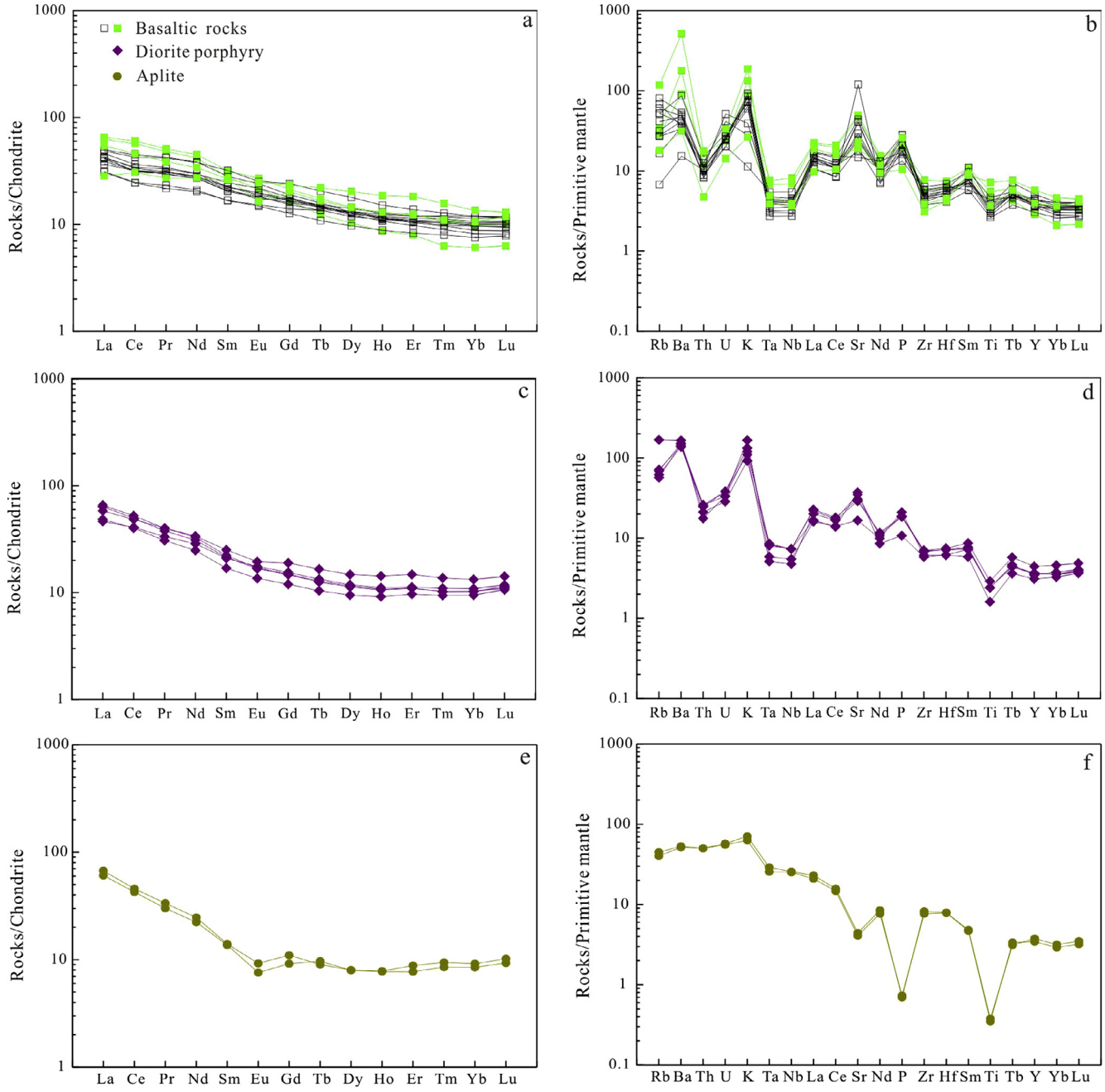

Fig. 4. Chondrite-normalized rare earth element (REE) and primitive mantle-normalized trace element diagrams (Sun and McDonough, 1989) for samples from the Qiaoxiahala deposit. (a) and (b) basaltic rocks; (c) and (d) diorite porphyry; (e) and (f) aplites. Data for volcanic rocks in the Qiaoxiahala deposit are from Chai et al. (2012).

$(Gd/Yb)_N$ = 1.18–2.71, mean 1.83; Fig. 4a). The samples have slightly negative Eu anomalies (δEu = 0.70–1.03, mean 0.96) and Ce anomalies (δCe = 0.88–1.10, mean 0.95).

Multi-element variation diagrams (Fig. 4b) of the volcanic rocks at Qiaoxiahala are characterized by an enrichment in large-ion lithophile elements (LILEs; e.g., Ba, K and Sr) relative to high field strength elements (HFSEs; i.e., Nb, Ta, Zr, Ti, Th and Y) and heavy rare earth element (HREEs; i.e., Yb and Lu), and display positive P anomalies.

5.1.2. Intrusive rocks

The diorite porphyry is characterized by SiO_2 contents of 54.65–60.83 wt.% and Al_2O_3 of 15.91–17.25 wt.%. All samples show elevated ($K_2O + Na_2O$) contents of 7.16–9.47 wt.%, Na_2O/K_2O ratios of 0.98–1.56 (Na_2O = 4.32–4.71 wt.%; K_2O = 2.78–4.78 wt.%), TiO_2 of 0.33–0.59 wt.% and P_2O_5 of 0.23–0.43 wt.%. The diorite porphyry has metaluminous A/NK ratios of 1.31–1.69 and A/CNK of 0.78–0.88. The diorites have Mg# of 27–35 and MgO of 1.50–3.14 wt.%.

The two aplite samples have SiO_2 contents of 80.55 and 83.02 wt.%, are metaluminous with A/NK of 1.09 and 1.15 and A/CNK of 0.87 and 0.92, with low TiO_2 (0.08 wt.%) and Al_2O_3 contents (8.48 and 9.99 wt.%). Total K_2O and Na_2O (Na_2O = 3.47 and 3.87 wt.%; K_2O = 1.90 and 2.13 wt.%) are 5.37 and 6.01 wt.% with Na_2O/K_2O ratios of 1.81 and 1.83. They have MgO and Mg# of 0.17–0.21 wt.% and 35–38, respectively.

Total REE contents (∑REE) of the diorite porphyry range from 63.5 to 82.5 ppm (mean 75.2 ppm) with LREE/HREE of 4.69–6.37 (mean 5.55). The $(La/Sm)_N$ ratio ranges from 2.21 to 2.97 (mean

2.66) whereas $(Gd/Yb)_N$ ranges from 1.26 to 1.45 (mean 1.40; Fig. 4c and e). The rocks are characterized by variable Eu anomalies (δEu = 0.88–0.96, mean 0.93) and weakly negative Ce anomalies (δCe = 0.98 and 1.02, mean 1.00). The aplite has ∑REE contents of 64.2 and 69.9 ppm (mean 67.0 ppm), $(La/Sm)_N$ of 4.45 and 4.80 (mean 4.62) and $(Gd/Yb)_N$ of 1.08 and 1.20 (mean 1.14), with LREE/HREE of 7.13 and 7.15 (mean 7.14). The aplite has negative Eu anomalies of 0.66 and 0.74 (mean 0.70) and slightly negative Ce anomalies (δCe = 0.91 and 0.94, mean 0.92).

The primitive mantle-normalized multi-element patterns (Fig. 4d) for the Qiaoxiahala diorite porphyry are characterised by enrichment of large ion lithophile elements (LILEs, e.g., Rb, Ba, K and Sr) and P relative to high field strength elements (HFSEs, e.g., Nb, Ta, Zr, Ti, Th and Y). The primitive mantle-normalized multi-element patterns for the aplite (Fig. 4f) are characterized by the Sr, P and Ti depletions and the K, Nd, Zr and Hf enrichments, as well as by the absence of significant Nb and Ta anomalies.

5.2. Zircon U-Pb age and REE geochemistry

5.2.1. Diorite porphyry

Most zircons from sample QX-043 are colorless or light-brown and euhedral with igneous oscillatory zoning, although some are anhedral and have low-luminescence rims (sp. 12; Fig. 5). The zircons are 50–80 μm (up to ca. 100 μm) long with length/width ratios of ca. 1:1–2:1. The zircons have U contents of 108–735 ppm (except sp. 6, U = 1048 ppm), Th of 26.8–699 ppm and Th/U ratios of 0.09–0.95, suggesting a magmatic origin. The chondrite-normalized REE patterns are similar to typical magmatic zircons (Fig. 6e), with elevated HREE/LREE ratios and pronounced positive Ce and minor negative Eu anomalies. Two strange lines for zircons (sp. 6; sp. 16; Fig. 6e) in the chondrite-normalized REE patterns, may be caused by apatite and/or fluid inclusions. Seven analyses of zircons yielded $^{206}Pb/^{238}U$ ages of 382.6 ± 6.2 Ma to 374.9 ± 6.4 Ma with a weighted mean age of 380.0 ± 4.0 Ma (MSDW = 0.19). Seven zircons yielded $^{206}Pb/^{238}U$ ages of 475.9 ± 6.3 Ma–461.8 ± 6.0 Ma (weighted mean age = 469.6 ± 4.8 Ma; MSDW = 0.48), whereas three zircons yielded $^{206}Pb/^{238}U$ ages of 508.9 ± 5.5 Ma–501.4 ± 10.0 Ma (weighted mean $^{206}Pb/^{238}U$ age = 505.7 ± 8.2 Ma; MSDW = 0.38). The older zircons are regarded as inherited, consistent with core-overgrowth structures of dark cores and banded rims in the CL images (sp. 9, 11, 12, 18; Fig. 5; Belousova et al., 2002). The age of 380 ± 4.0 Ma (MSDW = 0.19) is interpreted to be the emplacement age for the diorite porphyry (Fig. 6a and b; Table 3).

5.2.2. Aplite

Zircons from sample QX-055-1 are prismatic, colorless to iridescent, and translucent. The zircons are 50–100 μm long with length/width ratios = ca. 1:1–4:1. Cathodoluminescence (CL) images show that the zircons are mainly dark in color with weak magmatic oscillatory zoning and striping. On the other hand, some grains (sp. 1, 2, 4, 6, 12, 16 and 20; Fig. 5) have homogeneous cores of protolith zircons with low-luminescence rims. Uranium contents are between 257 and 1087 ppm (sp. 13, U = 66.1 ppm) and Th between 116 and 1576 ppm (sp. 13, Th = 22.5 ppm). The Th/U ratios range from 0.47 to 1.70, mean 0.83 (except sp. 13, Th/U = 0.34), suggesting a magmatic origin and possible Th enrichment. The chondrite-normalized REE patterns are characterized by LREE/HREE depletion and positive Ce anomalies (Fig. 6f), also indicative of a magmatic origin. The younger zircon population yielded a $^{206}Pb/^{238}U$ age of 331.1 ± 3.1 Ma (MSDW = 0.72; n = 8), whereas the older group yielded a $^{206}Pb/^{238}U$ age of 380.6 ± 5.7 Ma. The oldest zircon yielded a $^{206}Pb/^{238}U$ age of 427.4 ± 8.3 Ma (sp. 13; Fig. 5; Table 3). The 331 ± 3.1 Ma age is the most common and is interpreted to represent the aplite formation age (Fig. 6c and d), whereas the 427.4 ± 8.3 Ma and 380.6 ± 5.7 Ma ages represent inherited zircon ages with distinct REE composition from the youngest group (Fig. 6f).

5.3. Zircon Hf isotopic compositions

Eleven *in-situ* zircon Hf isotope analyses were performed on the diorite porphyry sample QX-043. The 383–375 Ma zircon

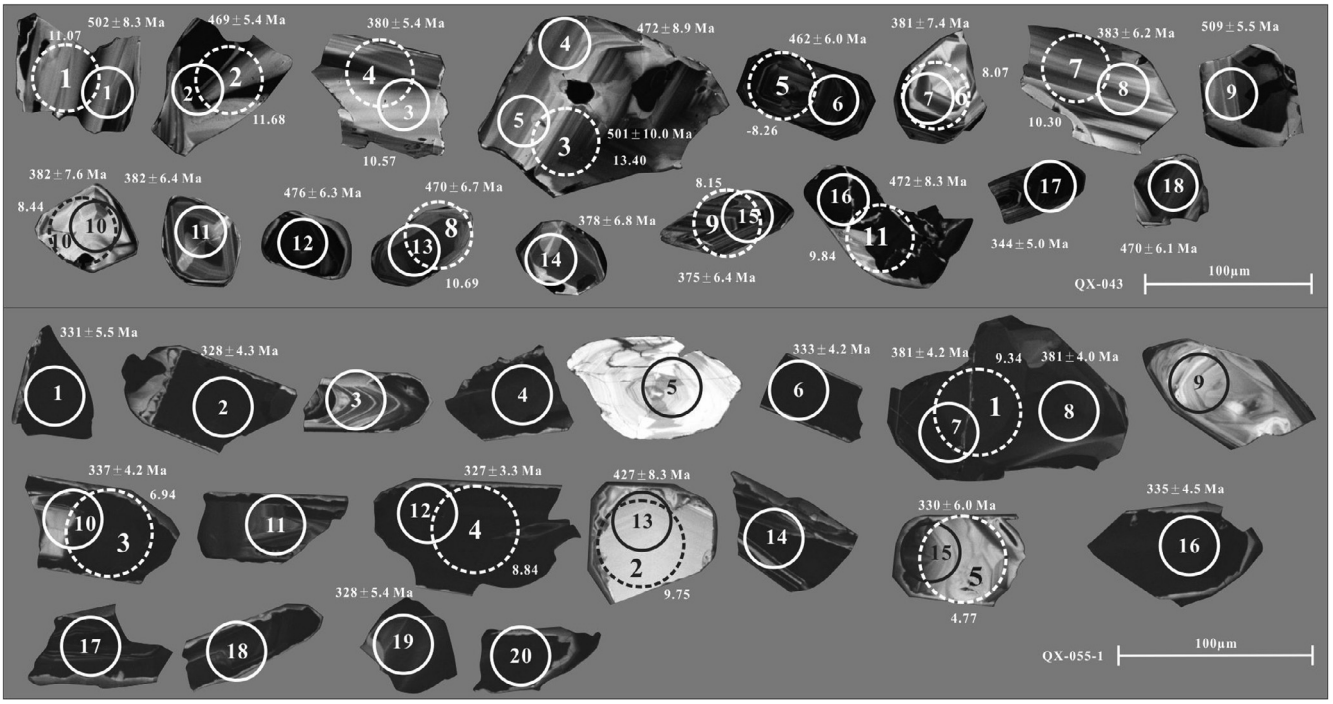

Fig. 5. Cathodoluminescence (CL) images for zircon grains from intrusive samples in the Qiaoxiahala deposit. Solid circles show spots for LA-ICP-MS U-Pb analyses in zircon grains and dotted circles show spots of Lu-Hf analyses in zircon grains.

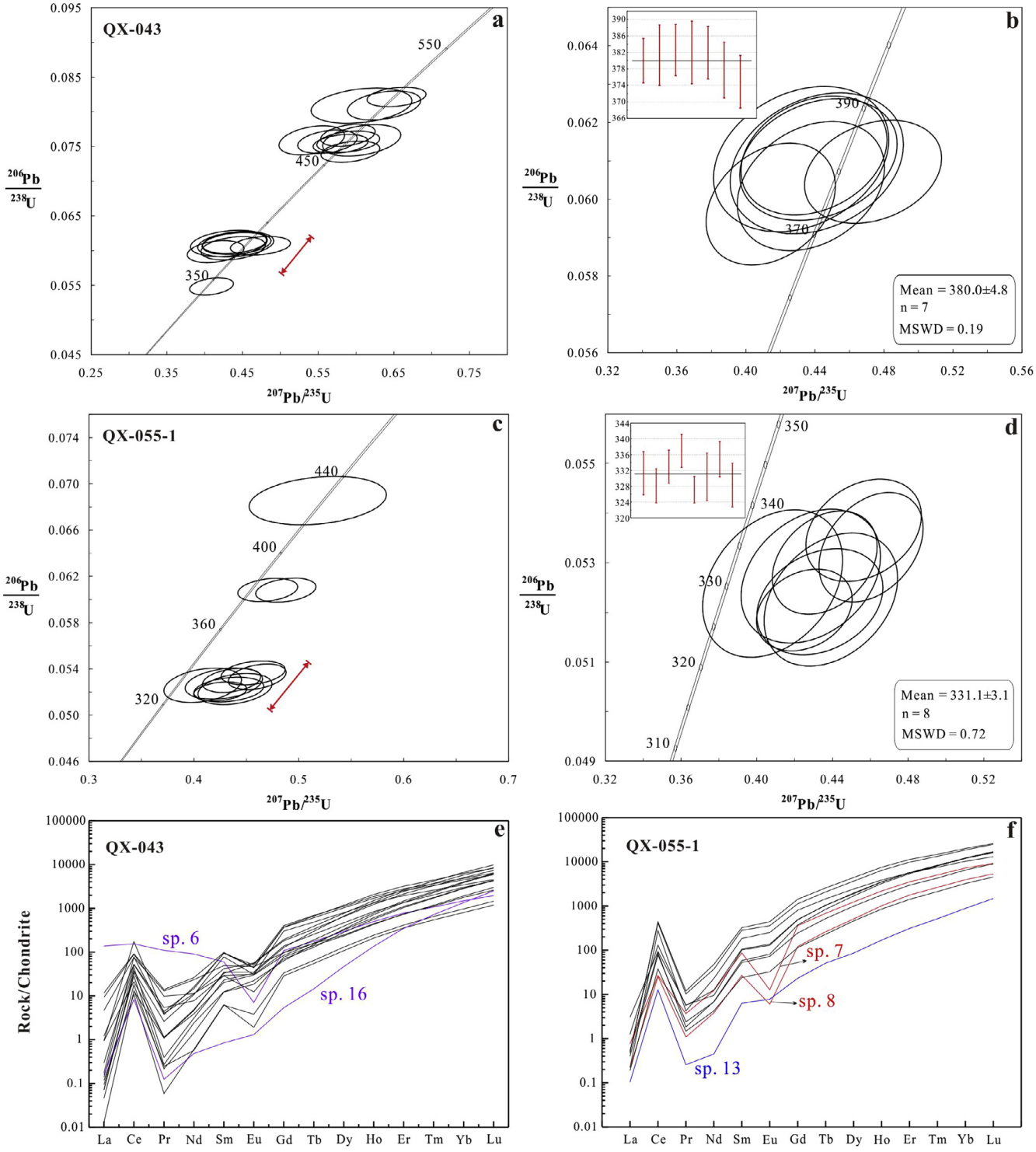

Fig. 6. (a)–(d) LA-ICP-MS zircon U-Pb concordia diagrams and $^{206}Pb/^{238}U$ weighted average ages for the Qiaoxiahala (a) and (b) diorite porphyry & (c) and (d) aplite. (e) and (f) Chondrite-normalized REE pattern of zircons for the Qiaoxiahala (e) diorite porphyry and (f) aplite.

population yielded $\varepsilon_{Hf}(t)$ of 8.07–10.57 and T^{C}_{DM} model ages of 863–703 Ma. The 472–462 Ma zircon population yielded positive $\varepsilon_{Hf}(t)$ of 9.84–11.68, with T^{C}_{DM} model ages of 820–701 Ma (except for one zircon with negative $\varepsilon_{Hf}(t) = -8.26$ and old T^{C}_{DM} model age = 1961 Ma). The $\varepsilon_{Hf}(t)$ and T^{C}_{DM} values for the 502–501 Ma zircon population are 11.07–13.40 and 765–616 Ma, respectively (Fig. 7a; Table 4).

Five *in-situ* zircon Hf isotope analyses were performed on the aplite sample QX-055-1. The 337–327 Ma zircon population yielded positive $\varepsilon_{Hf}(t)$ of 4.77–8.84 and T^{C}_{DM} model ages of 1035–773 Ma. The 381 and 427 Ma populations yielded $\varepsilon_{Hf}(t)$ of 9.34 and 9.75, and T^{C}_{DM} model ages of 782 Ma and 792 Ma (Fig. 7a; Table 4).

5.4. Strontium-Nd-Pb isotopes

The Sr-Nd and Pb isotopic data are reported in Tables 5 and 6 and illustrated in Fig. 7b–d. Initial isotopic ratios were back

Table 3
Zircon U-Pb isotopic data and calculated ages for intrusive rocks from the Qiaoxiahala deposit.

Spot No.	Concentration (ppm)		Ratios								Age (Ma)						Con. (%)
	Th	U	Th/U	$^{207}Pb/^{206}Pb$	1σ	$^{207}Pb/^{235}U$	1σ	$^{206}Pb/^{238}U$	1σ	Rho	$^{207}Pb/^{206}Pb$	1σ	$^{207}Pb/^{235}U$	1σ	$^{206}Pb/^{238}U$	1σ	
QX-043 Diorite porphyry																	
1	165	260	0.63	0.0568	0.0028	0.6370	0.0319	0.0809	0.0014	0.3407	483	109.2	500	19.8	502	8.3	99
2	80.3	670	0.12	0.0553	0.0023	0.5797	0.0240	0.0754	0.0009	0.2864	433	95.4	464	15.5	469	5.4	99
3	145	230	0.63	0.0527	0.0032	0.4737	0.0262	0.0607	0.0009	0.2637	317	140.7	394	18.1	380	5.4	96
4	37.3	138	0.27	0.0583	0.0035	0.6075	0.0341	0.0759	0.0015	0.3508	543	163.9	482	21.5	472	8.9	97
5	26.8	108	0.25	0.0545	0.0041	0.6073	0.0440	0.0809	0.0017	0.2852	394	170.4	482	27.8	501	10.0	96
6	545	1048	0.52	0.0576	0.0026	0.5925	0.0257	0.0743	0.0010	0.3111	522	98.1	472	16.4	462	6.0	97
7	68.0	119	0.57	0.0530	0.0042	0.4411	0.0331	0.0609	0.0012	0.2643	332	181.5	371	23.4	381	7.4	97
8	92.2	155	0.60	0.0523	0.0036	0.4395	0.0279	0.0611	0.0010	0.2631	302	125.0	370	19.7	383	6.2	96
9	160	658	0.24	0.0574	0.0023	0.6535	0.0257	0.0821	0.0009	0.2867	506	87.0	511	15.8	509	5.5	99
10	53.0	109	0.48	0.0503	0.0043	0.4320	0.0335	0.0610	0.0012	0.2637	209	188.9	365	23.8	382	7.6	95
11	76.1	168	0.45	0.0527	0.0036	0.4421	0.0301	0.0610	0.0010	0.2519	317	155.5	372	21.2	382	6.4	97
12	340	636	0.53	0.0554	0.0023	0.5893	0.0238	0.0766	0.0010	0.3388	428	94.4	470	15.2	476	6.3	98
13	289	439	0.66	0.0533	0.0025	0.5623	0.0260	0.0757	0.0011	0.3179	343	112.0	453	16.9	470	6.7	96
14	127	207	0.61	0.0532	0.0037	0.4377	0.0282	0.0603	0.0011	0.2862	345	157.4	369	19.9	378	6.8	97
15	301	371	0.81	0.0497	0.0032	0.4144	0.0247	0.0599	0.0010	0.2935	183	145.4	352	17.8	375	6.4	93
16	62.5	726	0.09	0.0511	0.0028	0.5415	0.0286	0.0759	0.0014	0.3442	256	123.1	439	18.9	472	8.3	92
17	699	735	0.95	0.0534	0.0026	0.4091	0.0191	0.0548	0.0008	0.3193	346	109.3	348	13.8	344	5.0	98
18	480	567	0.85	0.0560	0.0027	0.5897	0.0275	0.0757	0.0010	0.2875	450	107.4	471	17.5	470	6.1	99
QX-055 Aplite																	
1	1174	813	1.44	0.0569	0.0037	0.4286	0.0243	0.0527	0.0009	0.2978	500	144.4	362	17.3	331	5.5	91
2	1576	927	1.70	0.0585	0.0034	0.4333	0.0220	0.0522	0.0007	0.2662	546	158.3	366	15.6	328	4.3	89
3	200	249	0.80	0.0964	0.0055	0.7619	0.0375	0.0566	0.0008	0.2873	1567	102.8	575	21.6	355	4.9	52
4	481	791	0.61	0.0997	0.0054	0.7333	0.0375	0.0521	0.0006	0.2328	1618	101.1	559	22.0	328	3.8	47
5	60.3	93.8	0.64	0.2125	0.0154	1.8638	0.1466	0.0604	0.0016	0.3387	2924	118.4	1068	52.0	378	9.8	4
6	514	1087	0.47	0.0594	0.0027	0.4359	0.0183	0.0530	0.0007	0.3090	589	101.8	367	12.9	333	4.2	90
7	542	827	0.66	0.0578	0.0023	0.4876	0.0190	0.0608	0.0007	0.2911	520	87.0	403	12.9	381	4.2	94
8	441	638	0.69	0.0559	0.0023	0.4704	0.0189	0.0608	0.0007	0.2715	450	92.6	391	13.0	381	4.0	97
9	1767	965	1.83	0.1261	0.0048	0.9324	0.0366	0.0531	0.0006	0.2985	2056	67.4	669	19.2	334	3.8	33
10	250	461	0.54	0.0614	0.0029	0.4565	0.0201	0.0537	0.0007	0.2876	654	100.0	382	14.0	337	4.2	87
11	412	606	0.68	0.0702	0.0031	0.4935	0.0216	0.0508	0.0006	0.2822	1000	97.2	407	14.7	319	3.8	75
12	501	1056	0.47	0.0588	0.0023	0.4251	0.0167	0.0520	0.0005	0.2660	561	82.4	360	11.9	327	3.3	90
13	22.5	66.1	0.34	0.0554	0.0050	0.5181	0.0432	0.0685	0.0014	0.2419	428	201.8	424	28.9	427	8.3	99
14	552	957	0.58	0.0655	0.0027	0.4576	0.0184	0.0504	0.0006	0.3020	791	87.0	383	12.8	317	3.8	81
15	116	257	0.45	0.0561	0.0033	0.4084	0.0244	0.0526	0.0010	0.3124	454	134.2	348	17.6	330	6.0	94
16	600	1037	0.58	0.0623	0.0025	0.4604	0.0182	0.0533	0.0007	0.3466	685	87.0	385	12.6	335	4.5	86
17	589	709	0.83	0.0986	0.0041	0.7902	0.0321	0.0577	0.0007	0.2863	1598	77.8	591	18.2	362	4.1	51
18	836	721	1.16	0.0711	0.0027	0.5050	0.0197	0.0510	0.0006	0.2983	961	78.6	415	13.3	321	3.6	74
19	618	566	1.09	0.0609	0.0033	0.4392	0.0233	0.0523	0.0009	0.3195	635	113.9	370	16.4	328	5.4	88
20	479	764	0.63	0.1283	0.0049	0.9231	0.0335	0.0519	0.0006	0.3020	2076	67.3	664	17.7	326	3.5	31

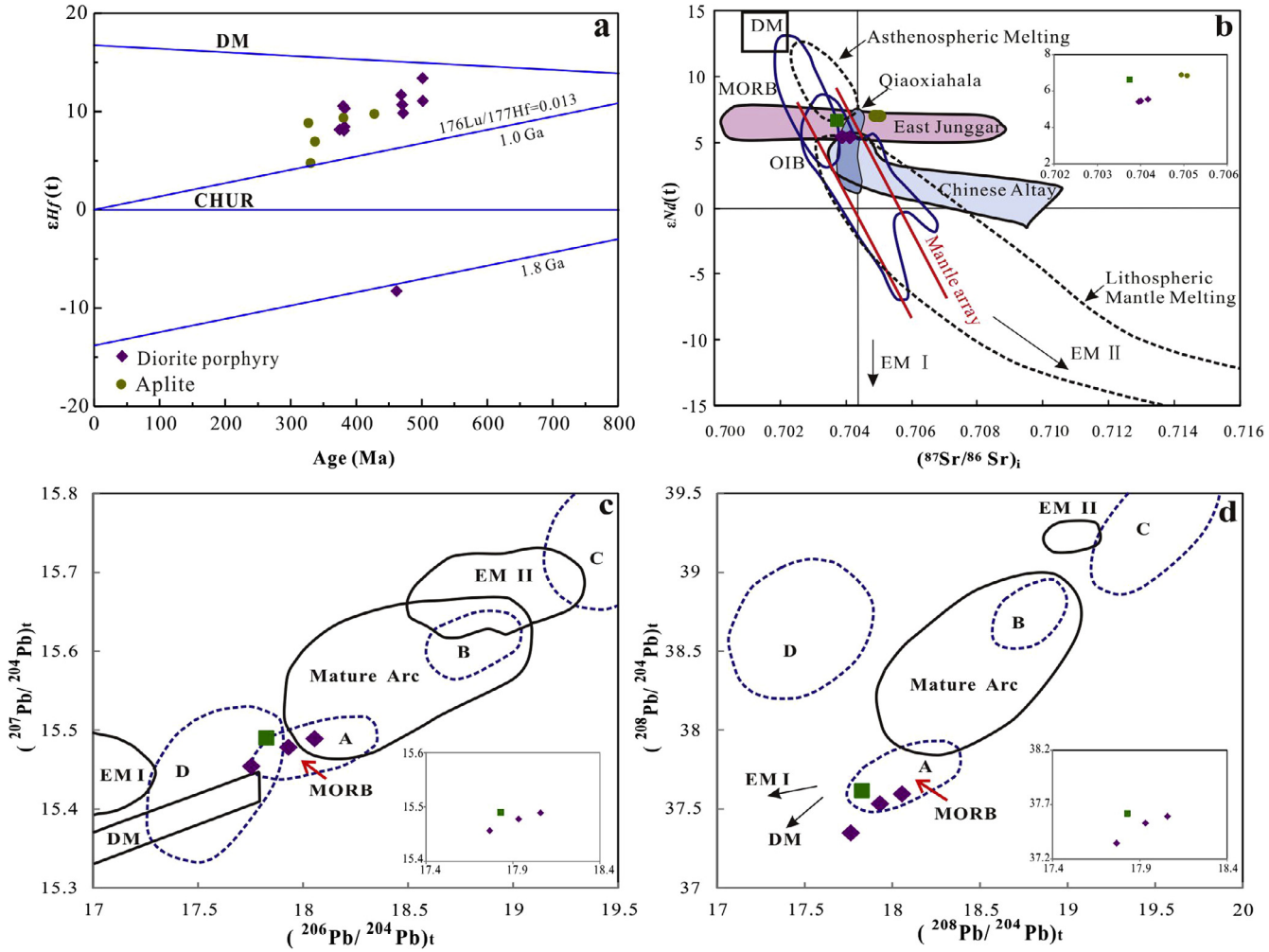

Fig. 7. (a) Plot of $\varepsilon_{Hf}(t)$ values vs. crystallizing ages for zircons from intrusive rocks of the Qiaoxiahala region. (b) $\varepsilon_{Nd}(t)$ vs. $(^{87}Sr/^{86}Sr)_i$ diagram (White and Hofmann, 1982; Zindler and Hart, 1986) for volcanic and intrusive rocks. Fields for asthenospheric and lithospheric mantle melting from Wilson (1989) and Davies and von Blanckenburg (1995); fields for MORB, OIB, EM I and EM II from Zindler and Hart (1986); data for Qiaoxiahala from Wan and Zhang (2006); data for East Junggar from Chen and Jahn (2004), Han et al. (1997), and Tang et al. (2006), data for Chinese Altai from Wang et al. (2009); mantle array from Arculus and Powell (1986) and Wilson (1989). (c) and (d) Plots of $(^{206}Pb/^{204}Pb)_t$ vs. $(^{207}Pb/^{204}Pb)_t$ and $(^{208}Pb/^{204}Pb)_t$ (Zartman and Doe, 1981) for volcanic and intrusive rocks. Abbreviations: EM I: enriched mantle I; EM II: enriched mantle II; OIB: ocean island basalts; DM: depleted mantle. Dashed lines (c) and (d) enclose average values from Zartman and Doe (1981), A = mantle; B = orogen; C = upper crust; and D = lower crust. Symbols as in Fig. 4.

Table 4
Zircon Lu-Hf isotopic data for intrusive rocks from the Qiaoxiahala deposit.

Spot No.	No. of zircon	Age (Ma)	σ	$^{176}Yb/^{177}Hf$	σ	$^{176}Lu/^{177}Hf$	σ	$^{176}Hf/^{177}Hf$	σ	εHf(0)	εHf(t)	σ	T_{DM} (Ma)	T^{C}_{DM} (Ma)	*f*Lu/Hf
QX-043 Diorite porphyry															
QX-043-1	1	502	8.3	0.041366	0.000800	0.001590	0.000030	0.282787	0.000013	0.54	11.07	0.45	669	765	−0.95
QX-043-2	2	469	5.4	0.016457	0.000277	0.000751	0.000011	0.282817	0.000014	1.58	11.68	0.48	613	701	−0.98
QX-043-3	5	501	10.0	0.017657	0.000385	0.000739	0.000014	0.282845	0.000013	2.59	13.40	0.45	573	616	−0.98
QX-043-4	3	380	5.4	0.063270	0.000258	0.002741	0.000011	0.282854	0.000013	2.89	10.57	0.47	592	703	−0.92
QX-043-5	6	462	6.0	0.032973	0.000247	0.001243	0.000008	0.282262	0.000017	−18.04	−8.26	0.61	1406	1961	−0.96
QX-043-6	7	381	7.4	0.048297	0.000279	0.002219	0.000014	0.282779	0.000016	0.24	8.07	0.57	693	863	−0.93
QX-043-7	8	383	6.2	0.053491	0.000704	0.002206	0.000033	0.282841	0.000012	2.44	10.30	0.41	602	722	−0.93
QX-043-8	13	470	6.7	0.030185	0.000473	0.001171	0.000016	0.282792	0.000015	0.69	10.69	0.52	656	765	−0.96
QX-043-9	15	375	6.4	0.068642	0.001350	0.003076	0.000055	0.282791	0.000014	0.66	8.15	0.51	692	853	−0.91
QX-043-10	10	382	7.6	0.049628	0.000450	0.002271	0.000021	0.282789	0.000017	0.61	8.44	0.61	679	840	−0.93
QX-043-11	16	472	8.3	0.015464	0.000096	0.000792	0.000005	0.282763	0.000010	−0.30	9.84	0.36	689	820	−0.98
QX-055-1 Aplite															
QX-055-1	7	381	4.2	0.092890	0.001345	0.003560	0.000050	0.282825	0.000015	1.86	9.34	0.52	650	782	−0.89
QX-055-2	13	427	8.3	0.013935	0.000247	0.000634	0.000010	0.282787	0.000015	0.51	9.75	0.52	653	792	−0.98
QX-055-3	10	337	4.2	0.082724	0.000349	0.003351	0.000013	0.282780	0.000013	0.27	6.94	0.46	714	902	−0.90
QX-055-5	12	327	3.3	0.045202	0.000543	0.001759	0.000019	0.282829	0.000013	2.02	8.84	0.46	612	773	−0.95
QX-055-4	15	330	6.0	0.115132	0.001137	0.004719	0.000043	0.282730	0.000015	−1.47	4.77	0.52	820	1035	−0.86

Table 5
Whole-rock Sr-Nd isotopic compositions for volcanic and intrusive rocks from the Qiaoxiahala deposit.

Spot No.	Lithology	Age (Ma)	Rb (ppm)	Sr (ppm)	$(^{87}Rb/^{86}Sr)m$	$(^{87}Sr/^{86}Sr)m$	±σ	$(^{87}Sr/^{86}Sr)i$	Sm (ppm)	Nd (ppm)	$(^{147}Sm/^{144}Nd)m$	$(^{143}Nd/^{144}Nd)m$	±σ	$(^{143}Nd/^{144}Nd)i$	$\varepsilon_{Nd}(t)$	T_{2DM} (Ma)	T_{DM} (Ma)
QX-052	Basalt	395	18.1	1050	0.0492	0.7040	0.000007	0.7037	4.88	21.0	0.1405	0.512836	0.000005	0.512473	6.7	596	658
QX-043	Diorite porphyry	380	43.5	643	0.1931	0.7051	0.000007	0.7040	3.41	15.4	0.1339	0.512760	0.000005	0.512427	5.4	687	764
QX-045	Diorite porphyry	380	36.1	786	0.1311	0.7047	0.000007	0.7040	2.59	11.6	0.1350	0.512757	0.000005	0.512421	5.3	696	658
QX-058	Diorite porphyry	380	39.2	613	0.1826	0.7051	0.000007	0.7042	3.85	15.8	0.1473	0.512796	0.000005	0.512430	5.5	683	816
QX-055-1	Aplite	331	28.5	93.3	0.8732	0.7091	0.000007	0.7049	2.14	11.5	0.1125	0.512807	0.000006	0.512563	6.9	531	520
QX-055-2	Aplite	331	25.6	86.4	0.8451	0.7091	0.000008	0.7051	2.09	10.4	0.1215	0.512826	0.000010	0.512563	6.9	531	538

calculated to the crystallization ages of intrusive rocks (this study) and the proposed age (ca. 395 Ma) of the Beitashan Formation volcanic rocks (based on the published age: >393 Ma).

Basalts in Qiaoxiahala yielded an initial $^{87}Sr/^{86}Sr$ value of 0.70374, $\varepsilon_{Nd}(t)$ of 6.6 and a two-stage depleted mantle Nd model age (T_{2DM}) = 594 Ma. Whole-rock Pb isotopic ratios for the basalts are 18.31 for $^{206}Pb/^{204}Pb$, 15.52 for $^{207}Pb/^{204}Pb$ and 38.04 for $^{208}Pb/^{204}Pb$. Calculated initial Pb isotope ratios of $(^{206}Pb/^{204}Pb)_t$, $(^{207}Pb/^{204}Pb)_t$ and $(^{208}Pb/^{204}Pb)_t$ are 17.83, 15.49 and 37.62, respectively.

The Qiaoxiahala diorite porphyry yielded initial $^{87}Sr/^{86}Sr$ ratios of 0.7040–0.7042, $\varepsilon_{Nd}(t)$ of 5.3–5.5 and T_{2DM} of 683–696 Ma. The $^{206}Pb/^{204}Pb$, $^{207}Pb/^{204}Pb$ and $^{208}Pb/^{204}Pb$ range from 18.92 to 19.20, 15.53 to 15.54 and 38.34 to 38.58, respectively. The calculated $(^{206}Pb/^{204}Pb)_t$, $(^{207}Pb/^{204}Pb)_t$ and $(^{208}Pb/^{204}Pb)_t$ range from 17.77 to 18.06, 15.46 to 15.49 and 37.34 to 37.59, respectively.

The Qiaoxiahala aplite has higher initial $^{87}Sr/^{86}Sr$ ratios of 0.7049–0.7051, higher $\varepsilon_{Nd}(t)$ of 6.85–6.86, lower T_{2DM} of 530.8–530.5 Ma and lower one-stage depleted mantle Nd model age (T_{DM}) of 538–520 Ma, compared to the Qiaoxiahala diorite porphyry.

6. Discussion

6.1. Timing of magmatism and mineralization

Fossil age evidence (crinoid stems, coral, shellfish and radiolarian) at Qiaoxiahala has been used to constrain the Beitashan Formation to the Early to Middle Devonian (ca. 398–385 Ma; Griffin et al., 2004). The Devonian age is consistent with the oldest intrusions reported in the Beitashan Formation, including SHRIMP U-Pb zircon ages of 381–376 Ma (Zhang et al., 2006) and LA-ICP-MS zircon U-Pb ages of 393–375 Ma (Xiang et al., 2009; Zhao et al., 2009; Lu et al., 2012; Yang et al., 2012; Li et al., 2014), indicating that the Beitashan Formation was formed older than ca. 393 Ma.

At least two intrusive phases have been identified at Qiaoxiahala, a Late Devonian phase that includes the diorite porphyry (ca. 380 Ma) and a late-Early Carboniferous phase that includes the aplite (ca. 331 Ma). Published age data compiled for the northern margin of East Junggar, as listed in Table 7 and illustrated in Fig. 8a, are broadly comparable to our new data, and support the existence of a voluminous Middle Devonian magmatic event (ca. 390–370 Ma) and a subordinate late-Early to early-Late- Carboniferous magmatic event (ca. 330–300 Ma).

High-resolution (HR)-ICP-MS molybdenite Re-Os dating had yielded 375.2 ± 2.6 Ma and 377.4 ± 4.3 Ma for the Qiaoxiahala Fe-Cu deposit (Zhang et al., 2012; Li et al., 2014), consistent with the formation age of the mineralization-related diorite porphyry (this study, ca. 380 Ma). The Late Devonian magmatic-metallogenic age at Qiaoxiahala is broadly coeval with the first phase of the regional metallogeny (ca. 380–370 Ma, the second phase at ca. 330–300 Ma) (Table 8; Fig. 8b), which are generally consistent with metallogenic periods of 378–374 Ma and 327–310 Ma by Yang et al. (2012).

6.2. Magma sources and petrogenesis

6.2.1. Basaltic rocks

The Nb/Y ratios of basaltic rocks at Qiaoxiahala are all below 0.7 and fall into the sub-alkaline basalt field and andesite or basalt field, indicating that the rocks are sub-alkaline (Fig. 9a). When plotted on the Ta/Yb versus Ce/Yb and Na_2O versus K_2O diagrams (Fig. 9b and c), all basaltic rocks fall in the calc-alkaline and high-K calc-alkaline basalt fields. The calc-alkaline basalt-andesite-dacite-rhyolite (BADR) volcanic series, are typical subduction-related arc

Table 6
Whole-rock Pb isotopic composition for volcanic and intrusive rocks from the Qiaoxiahala deposit.

Spot No.	Lithology	Age (Ma)	Pb (ppm)	Th (ppm)	U (ppm)	Th/U	$^{206}Pb/^{204}Pb$	$^{207}Pb/^{204}Pb$	$^{208}Pb/^{204}Pb$	$(^{206}Pb/^{204}Pb)t$	$(^{207}Pb/^{204}Pb)t$	$(^{208}Pb/^{204}Pb)t$
QX-052	Basalt	395	4.60	1.40	0.50	2.80	18.31	15.52	38.04	17.82	15.49	37.60
QX-043	Diorite porphyrite	380	2.50	2.20	0.80	2.75	19.20	15.53	38.58	17.77	15.46	37.34
QX-045	Diorite porphyrite	380	2.60	1.80	0.60	3.00	19.09	15.54	38.56	18.06	15.49	37.59
QX-058	Diorite porphyrite	380	3.60	2.10	0.80	2.63	18.92	15.53	38.34	17.93	15.48	37.53

Table 7
The geochronology data of intrusive rocks in the northern margin of East Junggar from the Early Devonian to the Late Carboniferous.

Samples	Location	Technical method	Age/Ma	Reference
Diorite porphyry	Qiaoxiahala	LA-ICP-MS U-Pb zircon age	380.0 ± 4.8	This study
Diorite porphyry	Qiaoxiahala	LA-ICP-MS U-Pb zircon age	379.2 ± 5.5	This study
Diorite porphyry	Qiaoxiahala	LA-ICP-MS U-Pb zircon age	377.6 ± 1.4	Zhang et al. (2012)
Diorite dyke	Qiaoxiahala	Hornblende Ar-Ar plateau age	378.1 ± 3.6	Ying, 2007)
Biotite diorite	Laoshankou	LA-ICP-MS U-Pb zircon age	380.5 ± 2.2	Liang et al. (submitted for publication)
Biotite diorite	Laoshankou	LA-ICP-MS U-Pb zircon age	379.3 ± 2.3	Lu et al. (2012)
Quartz syenite	Laoshankou	LA-ICP-MS U-Pb zircon age	376.3 ± 2.3	Liang et al. (submitted for publication)
Diorite porphyry	Laoshankou	LA-ICP-MS U-Pb zircon age	379.7 ± 3	Lu et al. (2012)
Diorite	Laoshankou	LA-ICP-MS U-Pb zircon	353.8 ± 1.9	Lu et al. (2012)
Syenite	Laoshankou	LA-ICP-MS U-Pb zircon	366.3 ± 1.9	Lu et al. (2012)
Granodiorite porphyry	Kalaxianger	LA-ICP-MS U-Pb zircon age	390.2 ± 4.9	Xiang et al. (2009)
Granodiorite porphyry	Kalaxianger	SHRIMP U-Pb zircon age	380.8 ± 5.7	Yan et al. (2006)
Quartz diorite	Yulekenhalasu	LA-ICP-MS U-Pb zircon age	382	Yang et al. (2014)
Mineralized diorite porphyry	Yulekenhalasu	LA-ICP-MS U-Pb zircon age	379	Yang et al. (2014)
Porphyritic quartz monzonite	Yulekenhalasu	LA-ICP-MS U-Pb zircon age	375–374	Yang et al. (2014)
Porphyritic granite	Yulekenhalasu	LA-ICP-MS U-Pb zircon age	381.6 ± 2.5	Zhao et al. (2009)
Porphyritic syenite	Halasu	LA-ICP-MS U-Pb zircon age	390.7 ± 2.4	Wu et al. (2015)
Porphyritic syenite	Halasu	LA-ICP-MS U-Pb zircon age	390.0 ± 1.9	Wu et al. (2015)
Quartz diorite	Halasu	LA-ICP-MS U-Pb zircon age	379.0 ± 2.8	Wu et al. (2015)
Quartz diorite	Halasu	LA-ICP-MS U-Pb zircon age	378.1 ± 2.4	Wu et al. (2015)
Granodiorite	Halasu	LA-ICP-MS U-Pb zircon age	378.0 ± 3.8	Wu et al. (2015)
Granodiorite porphyry	Halasu	LA-ICP-MS U-Pb zircon age	377.3 ± 2.8	Wu et al. (2015)
Quartz diorite	Halasu	LA-ICP-MS U-Pb zircon age	374.1 ± 3.3	Wu et al. (2015)
Quartz diorite	Halasu	LA-ICP-MS U-Pb zircon age	372.4 ± 3.3	Wu et al. (2015)
Alkali granite porphyry	Halasu	LA-ICP-MS U-Pb zircon age	327.0 ± 2.1	Wu et al. (2015)
Granodiorite porphyry	Halasu	SHRIMP U-Pb zircon age	381 ± 6	Wu et al. (2008)
Granodiorite porphyry	Halasu	SHRIMP U-Pb zircon age	375 ± 8.7	Xue et al. (2010)
Granodiorite porphyry	Halasu	SHRIMP U-Pb zircon age	371.8 ± 9.6	Xue et al. (2010)
Biotite adamellite	Bulgen Bei	U-Pb zircon	343 ± 3	Tong et al. (2012)
Alkali granite	Bulgen	U-Pb zircon	358 ± 4	Tong et al. (2012)
Alkali granite	Bulgen	U-Pb zircon	354 ± 4	Tong et al. (2012)
Moyite	Ertai	U-Pb zircon	319 ± 7	B. Han et al., (2006) and C. Han et al. (2006)
Granodiorite	Ertai Bei	SHRIMP U-Pb zircon	299 ± 9	Li et al. (2004)
Granitoid	Hadanxun pluton	Whole-rock Rb-Sr	300 ± 9	Zhou et al. (2006)
Monzonitic granite	Wutubulake	SHRIMP U-Pb zircon	360.1 ± 3.6	Zhou et al. (2009)
Mineraliztion granite porphyry	Xilekuduke	SIMS zircon U-Pb	329.6 ± 4.1	Long et al. (2009)
Granitoid	Areletuobie pluton	Whole-rock Rb-Sr	334.1 ± 9.5	Zhou et al. (2006)
Monzonite diorite porphyry	Kalasayi	SHRIMP U-Pb zircon age	376 ± 10	Zhang et al. (2006)

volcanic rocks (Green and Ringwood, 1968). On the Th-Ta-Hf/3 discrimination diagram (Fig. 10a), the majority of the basaltic rocks from the Qiaoxiahala deposit fall in the calc-alkaline arc basalt field. Whereas, the Th/Yb vs. Ta/Yb discrimination diagram (Fig. 10b) supports an island arc rather than a continental arc setting. The data that fall outside of the island arc field in Fig. 10b may be the result of fractional crystallization of Beitashan basaltic rocks. The basaltic rocks in Qiaoxiahala belong to a high-K calc-alkaline island arc basalts series, which may have three potential magma source components: (1) mantle wedge above the subducted slab, (2) subducted slab (melts and fluids), and (3) crust of the island arc (Defant and Drummond, 1990).

The relatively high Mg# (42–75, mean 56) suggests possible involvement of mantle wedge-derived melts (Rapp and Watson, 1995). Elevated Ce/Th (17.3–46.6) and Ba/Th ratios (123–2400), and the absence of pronounced negative Ce anomalies (0.88–1.10, mean 0.95) suggest the absence of significant subducted sediment input, as sources modified by subducted sediments are typically characterized by elevated Th, low Ce/Th (~8) and Ba/Th (~111), as well as negative Ce anomalies (Plank and Langmuir, 1998). The depleted Nb (1.94–5.80 ppm) contents in the basaltic rocks suggest the absence of Nb-enriched basalts in the Qiaoxiahala deposit, suggesting that melts derived from subducted oceanic crust have not been erupted in the arc (Hollings and Kerrich, 2000; Wyman et al., 2000). Moreover, the enrichment of LILEs and LREEs over HFSEs and HREEs indicate subduction-related metasomatism by the LILEs- and LREEs-bearing slab fluids (Schiano et al., 1995; Münker et al., 2004). On the $(Ta/La)_{PM}$ vs. $(Hf/Sm)_{PM}$ diagram all the basaltic rocks fall in the hydrated mantle source field, consistent with the influence of subduction-related fluids rather than slab melts (Fig. 12a; La Flèche et al., 1998).

Crustal assimilation can significantly modify the trace element and isotopic composition of mantle-derived magmas (Thirlwall et al., 1994). The basaltic rocks at Qiaoxiahala are characterized

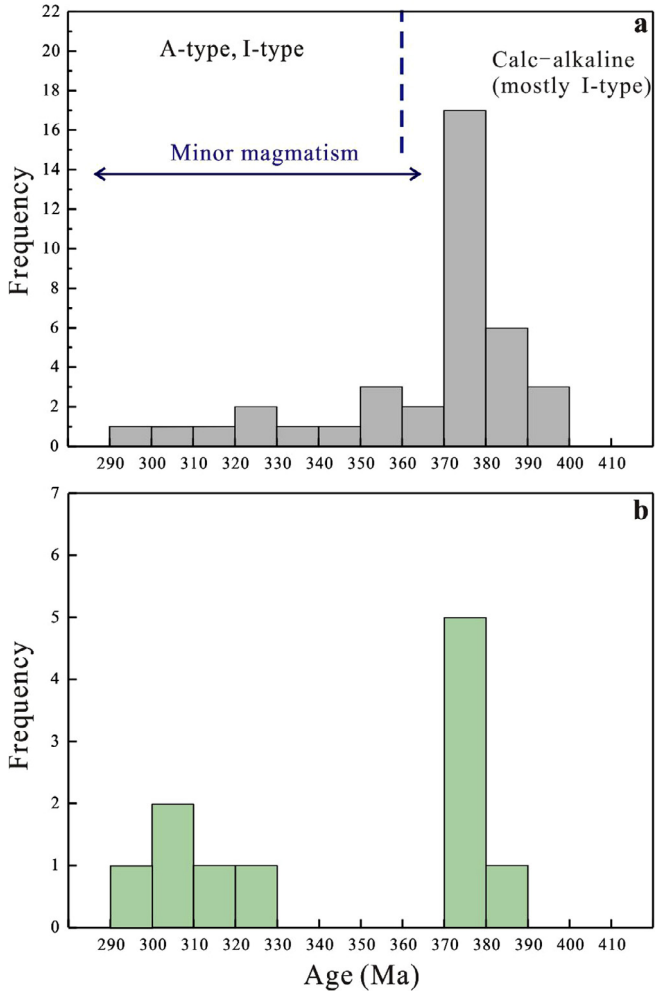

Fig. 8. Age histograms of the (a) magmatism and (b) mineralization in the northern margin of East Junggar.

by low Th, U, Rb and Nb/U, and higher Sr and Ba than average continental crust (Hofmann, 1988; Rudnick and Gao, 2003), suggesting that crustal assimilation was unlikely to be significant. Similarly, the negative Zr and Hf anomalies are not consistent with significant crustal inputs (Condie, 1989). The positive $\varepsilon_{Nd}(t)$ (6.6), low $(^{87}Sr/^{86}Sr)_i$ (0.7037) and MORB-like Pb isotopic signature (Fig. 7b–d) all suggest MORB-affinities and imply a MORB-like depleted mantle source with little or no crustal contamination.

As there is no evidence for significant crustal assimilation, another source is required for the high K in the basaltic rocks, possibly partial melting of K-rich minerals (such as hornblende and phlogopite) in the source region. Associated petrologic experiment has verified that these K-rich minerals are unstable in asthenosphere (Olafsson and Eggler, 1983), so the basaltic rocks may not come from asthenosphere. The low Rb/Sr and high Ba/Rb suggest a hornblende-rich source (J. Xu et al., 2001; Y.G. Xu et al., 2001). The La/Yb vs. Dy/Yb diagram (Fig. 12b) suggests that the basaltic rocks were generated from a mixture of melts derived from a garnet-bearing mantle and a spinel-bearing source (>90%). The relatively low Dr/Yb, La/Yb and LREE/HREE ratios suggest that the source region was likely in the spinel stability field. The depth of the spinel to garnet transition at the peridotite solidus is estimated to be ~75–80 km by McKenzie and O'Nions (1991) and Robinson and Wood (1998).

In summary, geochemical data suggest that the calc-alkaline/high-K calc-alkaline basaltic rocks were derived from partial melting of a MORB-like depleted mantle wedge in the hornblende-rich spinel stability field metasomatized by slab-derived fluids, with minor or no crustal contamination.

6.2.2. Diorite porphyry

The diorite porphyries at Qiaoxiahala are metaluminous (A/CNK = 0.78–0.88) and calc-alkaline (AR = 1.92–2.74), with Na_2O/K_2O of 0.98–1.56 and a mineralogy of hornblende ± apatite ± magnetite, consistent with typical I-type granitoids (Figs. 9d–f and 11a–d; Pitcher, 1997; Chappell and White, 2001). Furthermore, the enrichment of LILEs over HFSEs and HREEs and the negative Nb, Ta and Ti anomalies and positive Sr anomalies (Fig. 4d) are consistent with an arc setting (Pearce and Peate, 1995), which is supported by the Rb/30-Hf-Ta∗3 ternary diagram (Fig. 10c). On the A/CNK vs. A/NK and (La/Yb) vs. (Th/Yb) diagrams (Figs. 9e and 10d), the samples also show island arc rather than continental arc affinity.

Major, trace and rare element chemistry of the diorite porphyries are consistent with crystal fractionation from a basaltic parental magma. The decreasing MgO, CaO, $Fe_2O_3^T$, TiO_2 and Sr and the increasing K_2O and Ba with increasing SiO_2 suggest hornblende and plagioclase fractionation, whereas the lack of correlation between Zr/Hf and Nb/Ta, Zr/Hf and Sc suggests only minor clinopyroxene fractionation. Decreasing P_2O_5 with increasing SiO_2 probably reflects apatite fractionation. The fractional crystallization of accessory phases such as zircon can account for the depletion in Zr. Additionally, the distinct tendency of fractional crystallization is indicated by the negative correlation of Zr and Ni in Fig. 12c.

Crustal contamination and/or mixing as an important process for parental magma passed through the crust can produce some of their isotopic and incompatible trace element signatures. As illustrated in Fig. 12d and e, the correlations between Rb/Sr, MgO and $(^{87}Sr/^{86}Sr)_i$ are consistent with assimilation-fractionation

Table 8
The metallogenic ages of the deposits in the northern margin of East Junggar from the Early Devonian to the Late Carboniferous.

Samples	Location	Technical method	Age/Ma	Reference
Molybdenite	Halasu Cu deposit	Re-Os	378.3 ± 5.6	Yang et al. (2010)
Molybdenite	Halasu Cu deposit	Re-Os	376.9 ± 2.2	Wu et al. (2008)
Molybdenite	Yulekenhalasu Cu deposit	Re-Os	373.9 ± 2.2	Yang et al. (2012)
Molybdenite	Qiaoxiahala Fe-Cu deposit	Re-Os	375.2 ± 2.6	Li et al. (2014)
Molybdenite	Qiaoxiahala Fe-Cu deposit	Re-Os	377.4 ± 4.3	Zhang et al. (2012)
Molybdenite	Laoshankou Fe-Cu-Au deposit	Re-Os	383.2 ± 4.5	Li et al. (2015)
Molybdenite	Xilekuduke Cu–Mo deposit	Re-Os	327.1 ± 2.9	Long et al. (2011)
Quartz	Suoerkuduke Cu-Mo deposit	Rb-Sr	311 ± 46	Li and Chen, 2004)
Arsenopyrite	Saerbulake Au deposit	Pb-Pb	304 ± 7	Niu et al. (2006)
Sulfide	Kalatongke Cu-Ni deposit	Re-Os	290.2 ± 6.9	Zhang et al. (2005)
Sulfide	Kalatongke Cu-Ni deposit	Re-Os	305 ± 15	B. Han et al., (2006) and C. Han et al. (2006)

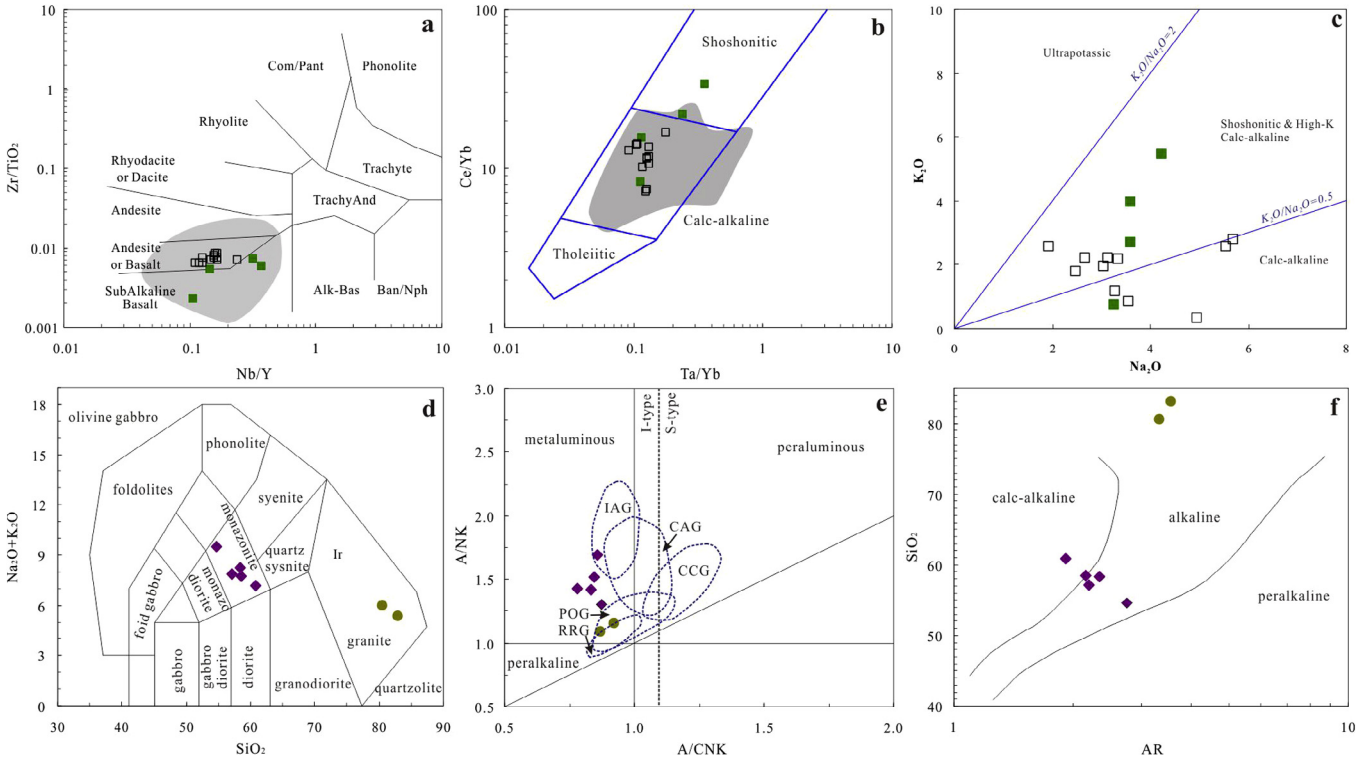

Fig. 9. Diagrams of (a) Nb/Y vs. Zr/TiO_2*0.0001 (Winchester and Floyd, 1977), (b) Ta/Yb vs. Ce/Yb (Pearce, 1982), (c) K_2O vs. Na_2O, (d) TAS (Middlemost, 1994), (e) A/CNK vs. A/NK (Maniar and Piccoli, 1989) and (f) SiO_2 vs. AR (Wright, 1969). Abbreviations: AR = $(Al_2O_3 + CaO + Na_2O + K_2O)/(Al_2O_3 + CaO - Na_2O - K_2O)$; Com/Pant: Comendite/Pantellerite; TrachyAnd: TrachyAndesite; Ban/Nph: Basanite/Nephelinite; Alk-Bas: alkaline-basalt; IAG: island arc granitoids; CAG: continental arc granitoids; CCG: continental collision granitoids; POG: post-orogenic granitoids; RRG: rift-related granitoids. Field in grey represents the volcanic rocks of the Beitashan Formation (Chai et al., 2012; Lu, 2012; Zhang et al., 2009). Data of volcanic rocks in the Qiaoxiahala deposit are from Chai et al. (2012). Symbols as in Fig. 4.

crystallization (AFC) and mixing processes. However, the lack of undercooled magmatic inclusions or mafic microgranular enclaves (MMEs) argues against mixing. The relatively high Th/U (2.14–3.14) and low Nb/Ta (14.9–16.2) ratios are consistent with addition of crustal material (Th/U = 6.0 and Nb/Ta = 12–14 for the crust; Rudnick and Gao, 2003). The presence of Cambrian (ca. 505 Ma) and Middle Ordovician (ca. 469 Ma) inherited zircons is also indicative of crustal inputs. Moreover, the wide range of $\varepsilon_{Hf}(t)$ with only one negative value (−8.26 with T^{C}_{DM} = 1961 Ma) for the zircons indicate the presence of ancient (about 2.0 Ga) crustal material, possibly the pre-existing sedimentary rocks with Precambrian zircons in the East Junggar (Li et al., 2006; Song et al., 2010; Lu et al., 2012).

The similar trace element ratios and Sr-, Nd-, Hf- and Pb-isotopic compositions of the Qiaoxiahala diorite porphyry and the basaltic rocks strongly indicate a common mantle wedge source modified by subducted fluids. This is supported by the positive $\varepsilon_{Hf}(t)$ and $\varepsilon_{Nd}(t)$, and the MORB-like Pb-isotopic signatures (Fig. 7a–d). The relative enrichments of LILEs and LREEs over HFSEs and HREEs, and the high Ba (960–1160 ppm) and Ba/Th (450–773, >170) suggest a slab-derived fluid influence (Plank and Langmuir, 1998). The high Ce/Th (13.67–16.67, >8), low Th/Yb (0.81–1.26, <2) and Th/La (0.14–0.16, <0.2) and absence of negative Ce anomaly (0.98–1.02, mean 1.00) and negative Nb anomaly suggest insignificant contribution from subducted oceanic crust and sediments (Plank and Langmuir, 1998; Hollings and Kerrich, 2000). In summary, the Qiaoxiahala diorite porphyry was likely the fractional crystallization product of parental basaltic magmas, with the addition of lower crustal materials and pre-exist sedimentary rocks with Precambrian zircons.

6.2.3. Aplite

The Qiaoxiahala aplite is metaluminous and alkaline (Fig. 9d–f). The rocks are similar to A-type granites in terms of their high SiO_2, $Na_2O + K_2O$, Zr, Nb, Ga, Sn, Y, Fe/Mg (>10), Ga/Al (>2.6), low CaO, Ba, Al_2O_3, MgO and Sr, and the flat chondrite normalized REE patterns with negative Eu and LREE-enrichment (Whalen et al., 1987; Eby, 1990). All Qiaoxiahala aplite samples plot in the A-type granite field on granite discrimination diagrams (Fig. 11a–d). Their zircons are Th-enriched, dark in color and contain Th-depleted, light-color margins with limited oscillatory zoning, typical of alkaline A-type granites (Xie et al., 2005). The rocks have higher SiO_2 and lower $Na_2O + K_2O$ than the average A-type granites (73–74 wt.% and 8.4–8.7 wt.%, respectively; Wu et al., 2007), possibly a result of the moderate silicic alteration.

In general, A-type granites can be formed by (1) partial melting of the crust, (2) fractional crystallization of mantle-derived melts, (3) AFC processes and (4) magma mixing between mantle- and crustal-derived melts (Clemens et al., 1986; Whalen et al., 1987; Eby, 1990, 1992; Turner et al., 1992). The high SiO_2 and extremely low MgO suggest that the aplite was unlikely to be generated by direct melting of the mantle, which would produce mafic to intermediate magmas (Taylor and McLennan, 1985). In the northern margin of East Junggar, there are very few mafic-ultramafic rocks that are closely related in time or space to the extensive A-type granitic magmatism (e.g., Bulgen, Kouan and Wutubulake A-type granite belts; Tong et al., 2006, 2012; Zhou et al., 2009; Shen et al., 2011), which implies that extensive fractional crystallization was unlikely to have happened.

The positive Zr and Hf anomalies in the aplite are consistent with a crustal contribution (Condie, 1989; Ketchum et al., 2013).

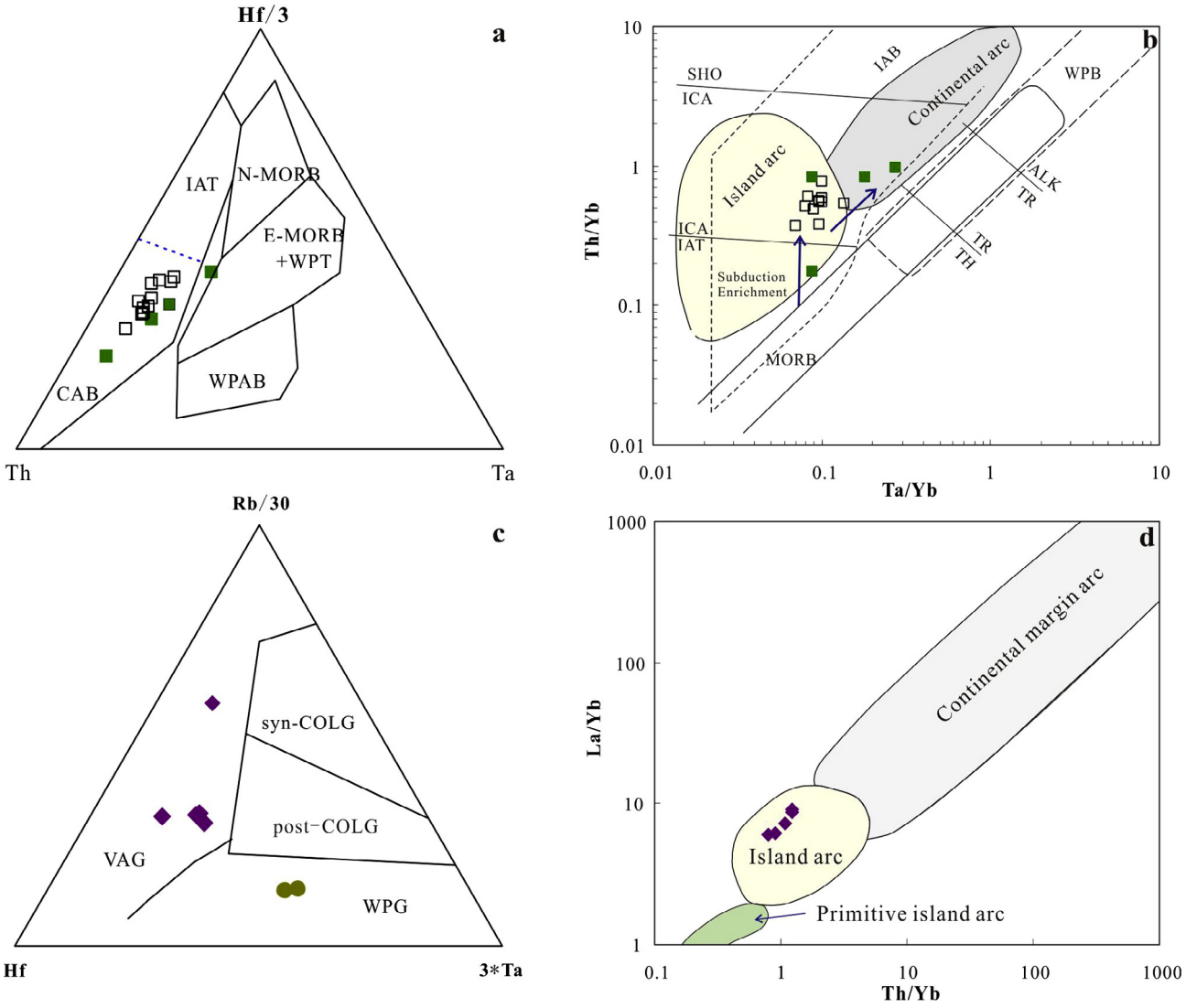

Fig. 10. (a) Th-Ta-Hf/3 (Wood, 1980) and (b) Th/Yb versus Ta/Yb discrimination diagram (Pearce and Norry, 1979) for volcanic rocks from the Qiaoxiahala deposit. (c) Rb/30-Hf-Ta∗3 (Harris et al., 1986) and (d) (La/Yb) vs. (Th/Yb) (Brown et al., 1984) discrimination diagrams for intrusive rocks from the Qiaoxiahala deposit. Abbreviations: WPB: within-plate basalts; MORB: mid-ocean ridge basalts; TH: tholeiites; TR: transitional basalt; ALK: alkaline basalts; N-MORB: normal MORB; E-MORB + WPT: enriched MORB and within plate tholeiites; WPAB: within plate alkaline basalts; IAT: island arc tholeiites; IAB: island arc basalts; ICA: island arc calc-alkaline series; SHO: shoshonitic series; CAB: calc-alkaline arc basalts; VAG: volcanic-arc granites; Syn-COLG: syn-collisional granites; Post-COLG: post collisional granites; WPG: within-plate granites. Symbols as in Fig. 4.

Besides, the presence of inherited zircons and the moderately high $(^{87}Sr/^{86}Sr)_i$ above the mantle array (Fig. 7b) also suggest a crustal input. Although crustal assimilation plus fractional crystallization or mixing processes are supported by the correlation of $(^{87}Sr/^{86}Sr)_i$ and MgO, Rb/Sr and $(^{143}Nd/^{144}Nd)_i$ in Fig. 12c–e, the positive $\varepsilon_{Hf}(t)$, $\varepsilon_{Nd}(t)$ and low T_{DM} (Fig. 7a and b) indicate crustal assimilation or magma mixing processes were unlikely to have played a pivotal role in the A1-type granite formation. An alternative formation mechanism is by partial melting of juvenile lower crustal materials generated by basaltic magmas underplating (Fig. 12f; Q. Wang et al., 2010; Shen et al., 2011). The Nb and Ta enrichments of the Qiaoxiahala aplite imply such juvenile crustal materials may be the early arc-related Nb-enriched basaltic rocks, which have been discovered by Zhang et al. (2006).

Previous studies have subdivided A-type granites into A1 and A2 types (Whalen et al., 1987; Eby, 1990; Pitcher, 1997). The A1 type is mantle-derived and emplaced in post-orogenic or anorogenic settings such as continental rifts or intraplate environments, whereas the A2 type is derived from partial melting of continental crust or underplated mafic crust and can be emplaced in a variety of tectonic settings. The Qiaoxiahala aplite shows A1 type geochemical affinities (Fig. 11e–h), suggesting a post-orogenic or anorogenic setting. On the A/CNK vs. A/NK (Fig. 9e) and Rb/30-Hf-Ta∗3 (Fig. 10c) diagrams, the aplite data also fall into the post-orogenic granite and within-plate granite fields, consistent with the rocks having formed in a post-orogenic extensional setting (Liégeois, 1998).

In summary, we propose the aplites were most likely produced by partial melting of the lower crust pre-existing basaltic rocks, caused by the underplating of mantle-derived melts, and accompanied by magma mixing.

6.3. Tectonic evolution and metallogenic implications

Previous regional geodynamic reconstructions (T. Wang et al., 2006; Zhang et al., 2006) suggested that Late Paleozoic magmatism in East Junggar evolved progressively from mostly I-type tholeiitic/calc-alkaline to A-type alkaline (Fig. 8a). This agrees with our

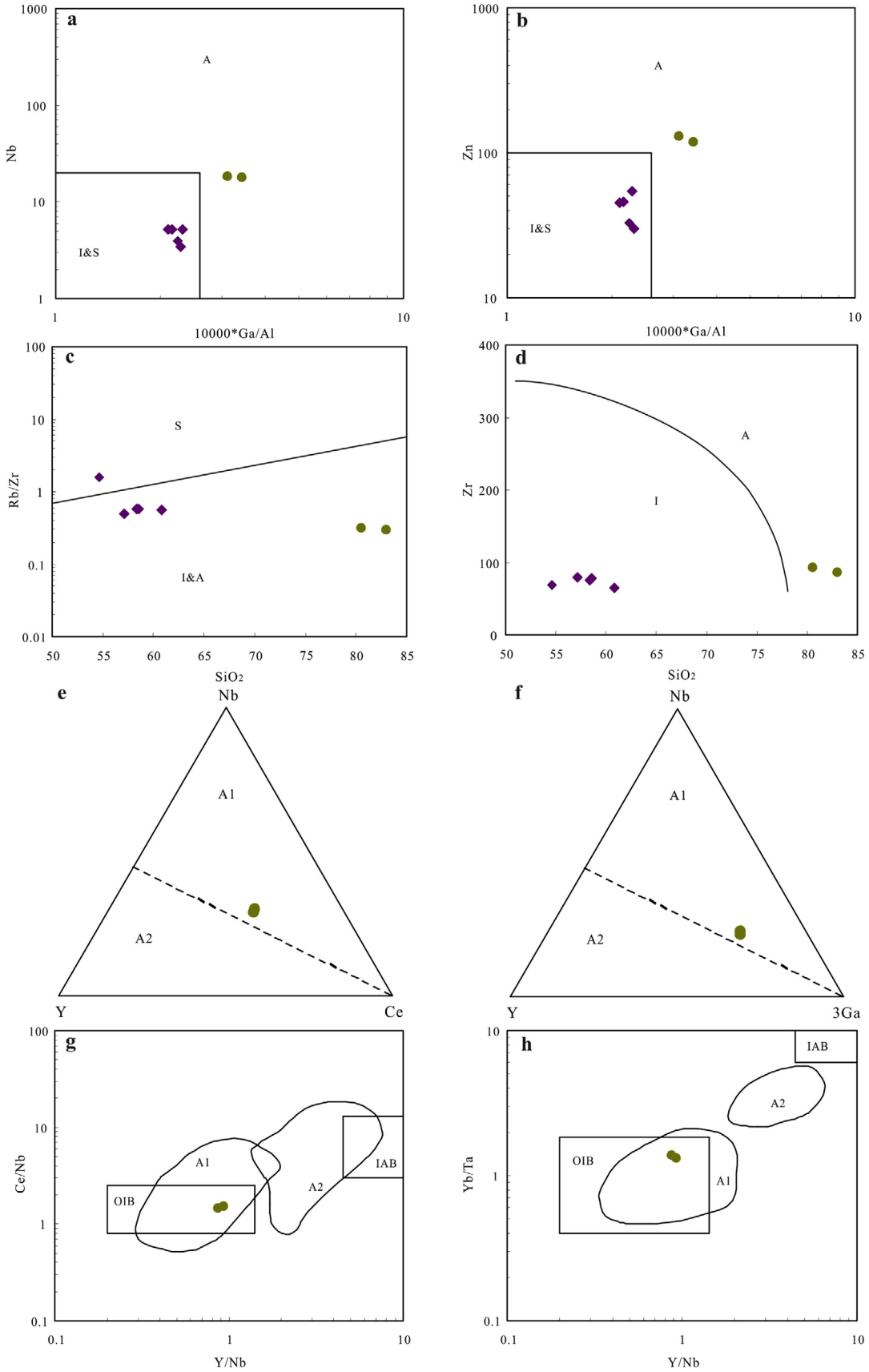

Fig. 11. (a) Nb vs. 10,000 Ga/Al and (b) Zn vs. 10,000 Ga/Al discrimination diagrams for I-, S- & M-type from A-type granitoids (Whalen et al., 1987). (c) Rb/Zr vs. SiO_2 discrimination diagram for I- & A-types granitoids from S-type rocks (Harris et al., 1986). (d) Zr vs. SiO_2 discrimination diagram for A-types granitoids from I-type rocks (Collins et al., 1982). (e) and (h) diagrams for discrimination of mantle-derived (A1) and crustal melting-derived (A2) granites (Eby, 1992). Symbols as in Fig. 4.

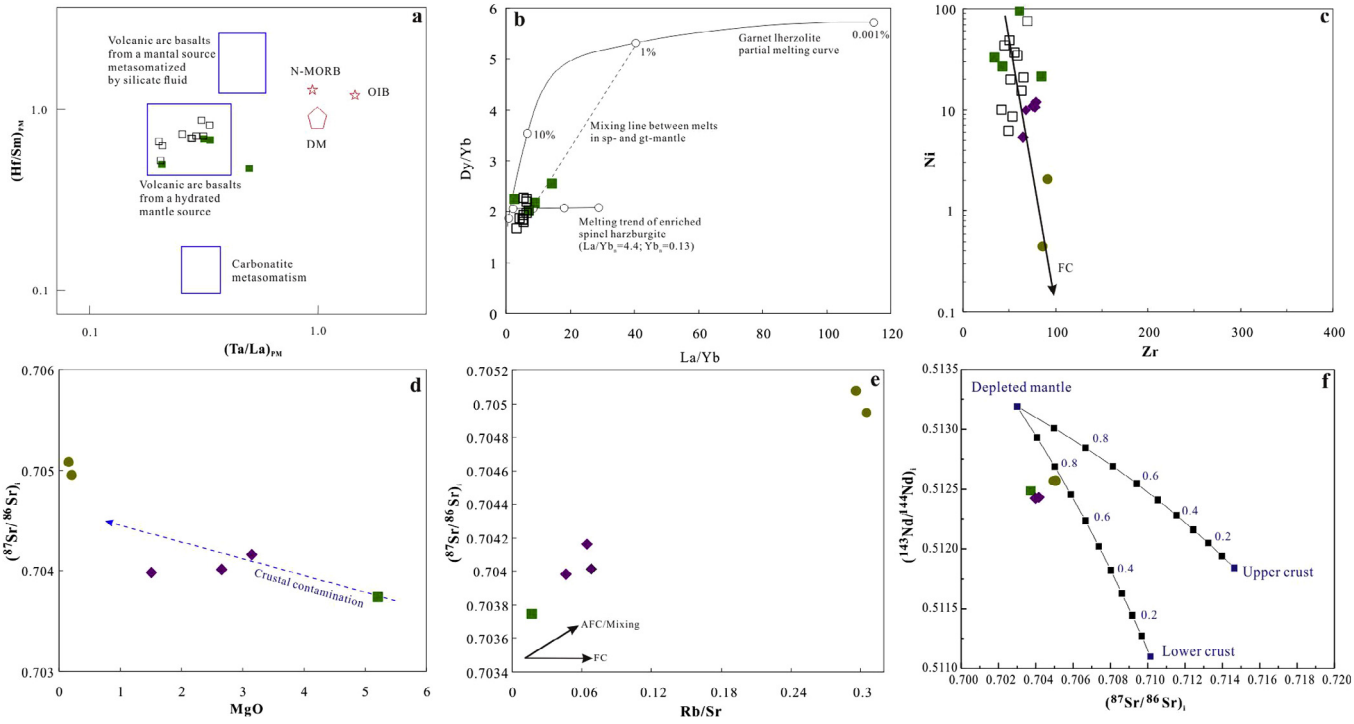

Fig. 12. (a) $(Hf/Sm)_{PM}$ vs. $(Ta/La)_{PM}$ discrimination diagram for basaltic rocks (after La Flèche et al., 1998). (b) Variation of La/Yb and Dy/Yb. The melting model, mode and partition coefficients are after J. Xu et al. (2001) and Y.G. Xu et al. (2001). (c) Zr vs. Ni showing possible fractional crystallization (FC) and assimilation-fractional crystallization (AFC) trends. (d) MgO vs. $(^{87}Sr/^{86}Sr)_i$ and (e) Rb/Sr vs. $(^{143}Nd/^{144}Nd)_i$ diagram. (f) $(^{87}Sr/^{86}Sr)_i$ vs. $(^{143}Nd/^{144}Nd)_i$ diagram showing the mixing modeling. Symbols as in Fig. 4.

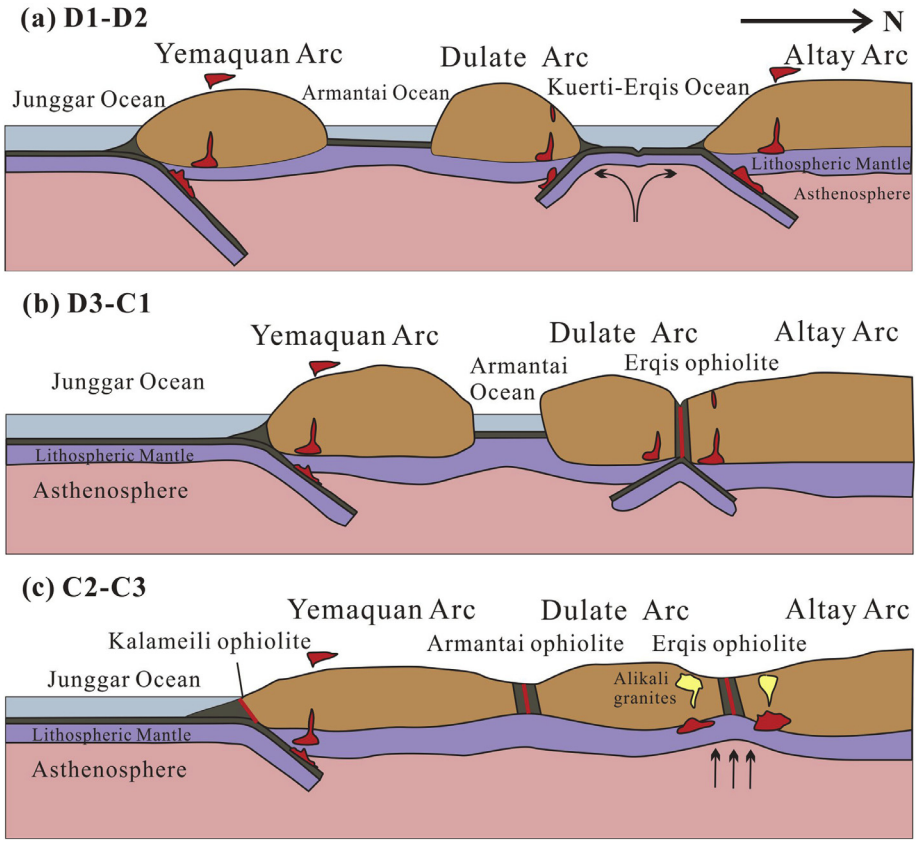

Fig. 13. Schematic tectonic model of the Early Devonian to Late Carboniferous northern Junggar and southern Altay terranes.

finding, in which the Middle Devonian basaltic rocks are calc-alkaline island arc basalts, whereas the Late Devonian (ca. 380 Ma) diorite porphyry are I-type island arc-related calc-alkaline, and the late-Early Carboniferous (ca. 331 Ma) aplite is A1-type alkaline and formed in a post-orogenic extension-related setting.

Previous studies (Long et al., 2012; Xu et al., 2013) have suggested that during the Early Devonian to Middle Devonian, the Dulate magmatic arc formed as a result of the southward subduction of the Kuerti-Erqis Ocean, whereas the northward subduction of the Kuerti-Erqis Ocean may have formed the southern Altay magmatic arc (Fig. 13a). The 390–370 Ma arc-related magmatism in the northern margin of East Junggar, including the Qiaoxiahala diorite porphyry, occurred in this period with synchronous arc-related Fe-Cu (-Au) mineralization, including the Qiaoxiahala Fe-Cu deposit, Laoshankou Fe-Cu-Au deposit and the arc-related Halasu, Yulekenhalasu and Kakasayi porphyry Cu deposits (Yao et al., 2007; Zhao et al., 2009; Yang et al., 2014; Wu et al., 2015).

The transition from the Middle Devonian Beitashan Formation coastal-shallow marine sedimentary facies to the Upper Devonian Jiangzierkuduke Formation continental sedimentary facies in East Junggar indicates that the Kuerti-Erqis Ocean (a branch of the Paleo-Asian Ocean) may have been completely closed. The consequent collision between the Chinese Altay and East Junggar terranes may have led to the Late Devonian tectonic uplift (The Regional Stratigraphic Chart of Xinjiang, 1983; Liang et al., submitted for publication). The Lower Carboniferous Nanmingshui Formation is dominated by continental arc volcanic rocks and coastal sedimentary rocks deposited in a fan delta to coastal plain environment (Pang et al., 2009). The local transformation from continental to coastal sedimentary rocks may reflect sea-level rise, caused by a possible extension environment in the Early Carboniferous. Moreover, no major magmatism occurred after 370 Ma (Fig. 8a), and there are only minor ophiolites younger than 360 Ma reported in the Erqis suture zone (Tong et al., 2012). All these observations support that the syn-collision between the Chinese Altay and East Junggar was nearly ended during the late-Late Devonian (370–360 Ma) and was followed by a period of post-collisional tectonics and intraplate extension.

B. Han et al., (2006) and C. Han et al. (2006) proposed that the post-collision environment ran from ca. 330 to 265 Ma (peaking at ca. 330–310 Ma and 305–280 Ma). However, several recent studies have changed the duration to ca. 360–290 Ma (Zhou et al., 2009) and ca. 355–318 Ma (T. Wang et al., 2010), consistent with post-collision environment starting in the Early Carboniferous (~360 Ma; Fig. 13b), corresponding to the inference above that the syn-collision ended during the Late Devonian and then turned to post-collision. Based on amount of previous researches, two major post-collisional magmatic phases: ca. 360–330 Ma and 330–290 Ma were divided (Fig. 8a). The 360–330 Ma magmatism for the earlier stage of the post-collisional event in the region occurred without significant synchronous mineralization, whereas the later stage 330–290 Ma magmatism for the later stage of the post-collision is associated with coeval Cu-Mo mineralization including the Suoerkuduke skarn Cu-Mo deposit (Wan et al., 2014; Zhao et al., 2015) and the Xilekuduke porphyry Cu-Mo deposit (L. Long et al., 2010; Long et al., 2011). The difference between the two stages may be explained by the fact that in the earlier stage the extension had just started and was weak, resulting in weaker magmatism and limited mineralization. In the later stage, the Chinese Altay-East Junggar was in a transitional period and the extension became more intense, which resulted in extensive magmatism and mineralization.

The Qiaoxiahala aplite (331 ± 3.1 Ma), which belongs to the intraplate post-orogenic extension A1-type granites, indicates that by the late-Early Carboniferous (ca. ~330 Ma) intraplate tectonics dominated in the Qiaoxiahala region. Combined with the previously reported post-collisional alkaline to calc-alkaline granitic magmatism (ca. 330–290 Ma) in the region (Fig. 8a; Table 7), we suggest that East Junggar was in a post-collision to intraplate tectonic transition during the late-Early to Late Carboniferous (Fig. 13c; Liégeois, 1998). And the various tectonic settings of different areas in East Junggar during this transition period may represent the accretion-collision of multiple-subduction systems (Coleman, 1989; Windley et al., 2007; Xiao et al., 2009).

7. Conclusions

(1) Zircon U-Pb dating yielded two intrusive phases at Qiaoxiahala: ca. 380 Ma (diorite porphyry) and ca. 331 Ma (aplite).
(2) The Middle Devonian basaltic rocks at Qiaoxiahala are (high-K) calc-alkaline island arc basaltic rocks, generated from partial melting of a MORB-like depleted mantle wedge metasomatized by slab-derived fluids, with little evidence of crustal contamination.
(3) The diorite porphyry is metaluminous, I-type island arc-related calc-alkaline, probably derived from the same magma source as the basaltic rocks. The various rock types may have been products of fractional crystallization and crustal contamination.
(4) The aplite is an A1-type (alkaline) and related to post-orogenic extension. The rocks may have formed by partial melting of pre-existing basaltic rocks in the lower crust, caused by the underplating of mantle-derived melts, and accompanied by magma mixing.
(5) Age and geochemical data of the volcanic and intrusive rocks at Qiaoxiahala suggest that East Junggar was in an island arc setting during the Early to Middle Devonian. The collision between East Junggar and southern Altay probably occurred in the Late Devonian (ca. 370–360 Ma), followed by the Early Carboniferous post-collisional tectonics and late-Early to Late Carboniferous (ca. 330–290 Ma) intraplate extensional tectonics.
(6) The Early to Middle Devonian arc-related magmatism (390–370 Ma) in the northern margin of East Junggar occurred with synchronous arc-related Fe-Cu (-Au) occurrences and the arc-related porphyry Cu mineralization, whereas the 330–290 Ma magmatism for the later stage of the post-collision is associated with synchronous Cu-Mo mineralization. However, the post-orogenic magmatism at Qiaoxiahala (ca. 330 Ma) is barren of mineralization.

Acknowledgments

This study was funded by the Chinese National Basic Research 973 Program (2014CB440802 and 2014CB448000) and the Creative and Interdisciplinary Program, CAS (Y433131A07). We thank Profs. Jinlong Ma and Xianglin Tu and Dr. Congying Li (State Key Laboratory of Isotope Geochemistry, GIGCAS) for the Sr-Nd isotopic analysis, as well as Prof. Liang Qi (IGCAS) for the whole-rock geochemical analysis. Long Chen and Zhenjiang Liu are thanked for their field support. Dr. Jinsheng Han, Weifeng Zhang, Hongjun Jiang and Wanjian Lu are acknowledged for their constructive and insightful discussions in the manuscript preparation. The manuscript benefited significantly from critical reviews and insightful comments by two anonymous reviewers. Detailed editorial suggestions from Sanghoon Kwon also helped improve the quality of the paper.

References

Andersen, T., 2002. Correction of common lead in U-Pb analyses that do not report Pb-204. Chem. Geol. 192, 59–79.

Arculus, R.J., Powell, R., 1986. Source component mixing in the regions of arc magma generation. J. Geophys. Res.: Solid Earth (1978–2012) 91, 5913–5926.

Belousova, E., Griffin, W.L., O'reilly, S.Y., Fisher, N., 2002. Igneous zircon: trace element composition as an indicator of source rock type. Contrib. Miner. Petrol. 143, 602–622.

Black, L.P., Kamo, S.L., Allen, C.M., Aleinikoff, J.N., Davis, D.W., Korsch, R.J., Foudoulis, C., 2003. TEMORA 1: a new zircon standard for Phanerozoic U-Pb geochronology. Chem. Geol. 200, 155–170.

Blichert-Toft, J., Albarède, F., 1997. The Lu-Hf isotope geochemistry of chondrites and the evolution of the mantle-crust system. Earth Planet. Sci. Lett. 148, 243–258.

Brown, G.C., Thorpe, R.S., Webb, P.C., 1984. The geochemical characteristics of granitoids in contrasting arcs and comments on magma sources. J. Geol. Soc. 141, 413–426.

Cai, K., Sun, M., Yuan, C., Zhao, G., Xiao, W., Long, X., Wu, F., 2010. Geochronological and geochemical study of mafic dykes from the northwest Chinese Altai: implications for petrogenesis and tectonic evolution. Gondwana Res. 18, 638–652.

Chai, F.M., Yang, F.Q., Liu, F., Geng, X.X., Lu, S.J., Jiang, L.P., Zang, M., Chen, B., 2012. Geochronology and genesis of volcanic rocks in Beitashan Formation at the northern margin of the Junggar, Xinjiang. Acta Petrol. Sin. 28, 2183–2198 (in Chinese with English abstract).

Chappell, B., White, A.J.R., 2001. Two contrasting granite types: 25 years later. Aust. J. Earth Sci. 48, 489–499.

Chen, B., Jahn, B.M., 2002. Geochemical and isotopic studies of the sedimentary and granitic rocks of the Altai orogen of northwest China and their tectonic implications. Geol. Mag. 139, 1–13.

Chen, B., Jahn, B.M., 2004. Genesis of post-collisional granitoids and basement nature of the Junggar Terrane, NW China: Nd–Sr isotope and trace element evidence. J. Asian Earth Sci. 23, 691–703.

Clemens, J., Holloway, J., White, A., 1986. Origin of an A-type granite: experimental constraints. Am. Mineral. 71, 317–324.

Coleman, R.G., 1989. Continental growth of northwest China. Tectonics 8, 621–635.

Collins, W., Beams, S., White, A., Chappell, B., 1982. Nature and origin of A-type granites with particular reference to southeastern Australia. Contrib. Miner. Petrol. 80, 189–200.

Condie, K.C., 1989. Geochemical changes in basalts and andesites across the Archean-Proterozoic boundary: identification and significance. Lithos 23, 1–18.

Davies, J.H., von Blanckenburg, F., 1995. Slab breakoff: a model of lithosphere detachment and its test in the magmatism and deformation of collisional orogens. Earth Planet. Sci. Lett. 129, 85–102.

Defant, M.J., Drummond, M.S., 1990. Derivation of some modern arc magmas by melting of young subducted lithosphere. Nature 347, 662–665.

Eby, G.N., 1990. The A-type granitoids: a review of their occurrence and chemical characteristics and speculations on their petrogenesis. Lithos 26, 115–134.

Eby, G.N., 1992. Chemical subdivision of the A-type granitoids: petrogenetic and tectonic implications. Geology 20, 641–644.

Green, T.H., Ringwood, A., 1968. Genesis of the calc-alkaline igneous rock suite. Contrib. Miner. Petrol. 18, 105–162.

Griffin, W., Belousova, E., Shee, S., Pearson, N., O'reilly, S., 2004. Archean crustal evolution in the northern Yilgarn Craton: U-Pb and Hf-isotope evidence from detrital zircons. Precambr. Res. 131, 231–282.

Griffin, W., Pearson, N., Belousova, E., Jackson, S., Van Achterbergh, E., O'Reilly, S.Y., Shee, S., 2000. The Hf isotope composition of cratonic mantle: LA-MC-ICPMS analysis of zircon megacrysts in kimberlites. Geochim. Cosmochim. Acta 64, 133–147.

Han, B., Ji, J., Song, B., Chen, L., Zhang, L., 2006. Late Paleozoic vertical growth of continental crust around the Junggar Basin, Xinjiang, China (Part I): timing of post-collisional plutonism. Acta Petrol. Sin. 22, 1077–1086 (in Chinese with English abstract).

Han, B.F., Wang, S.G., Jahn, B.M., Hong, D.W., Kagami, H., Sun, Y.L., 1997. Depleted-mantle source for the Ulungur River A-type granites from North Xinjiang, China: geochemistry and Nd–Sr isotopic evidence, and implications for Phanerozoic crustal growth. Chem. Geol. 138, 135–159.

Han, C., Xiao, W., Zhao, G., Qu, W., Mao, Q., Du, A., 2006. Re-Os isotopic analysis of the Kalatongke Cu-Ni sulfide deposit, northern Xinjiang, NW China, and its geological implication. Acta Petrol. Sin. 22, 163–170.

Harris, N.B., Pearce, J.A., Tindle, A.G., 1986. Geochemical characteristics of collision-zone magmatism. Geol. Soc. Lond. Spec. Publ. 19, 67–81.

Hofmann, A.W., 1988. Chemical differentiation of the Earth: the relationship between mantle, continental crust, and oceanic crust. Earth Planet. Sci. Lett. 90, 297–314.

Hollings, P., Kerrich, R., 2000. An Archean arc basalt–Nb-enriched basalt–adakite association: the 2.7 Ga Confederation assemblage of the Birch-Uchi greenstone belt, Superior Province. Contrib. Miner. Petrol. 139, 208–226.

Huang, H., Zhang, Z., Santosh, M., Zhang, D., 2014. Geochronology, geochemistry and metallogenic implications of the Boziguo'er rare metal-bearing peralkaline granitic intrusion in South Tianshan, NW China. Ore Geol. Rev. 61, 157–174.

Jackson, S.E., Pearson, N.J., Griffin, W.L., Belousova, E.A., 2004. The application of laser ablation-inductively coupled plasma-mass spectrometry to in situ U-Pb zircon geochronology. Chem. Geol. 211, 47–69.

Jahn, B.M., Wu, F.Y., Chen, B., 2000. Massive granitoid generation in Central Asia: Nd isotope evidence and implication for continental growth in the Phanerozoic. Episodes 23, 82–92.

Ketchum, K.Y., Heaman, L.M., Bennett, G., Hughes, D.J., 2013. Age, petrogenesis and tectonic setting of the Thessalon volcanic rocks, Huronian Supergroup, Canada. Precambr. Res. 233, 144–172.

La Flèche, M., Camire, G., Jenner, G., 1998. Geochemistry of post-Acadian, Carboniferous continental intraplate basalts from the Maritimes Basin, Magdalen islands, Quebec, Canada. Chem. Geol. 148, 115–136.

Li, H.Q., Chen, F.W., 2004. Isotopic Geochronology of Regional Mineralization in Xinjiang, China. Geological Publishing House, Beijing, pp. 68–82 (in Chinese with English abstract).

Li, J., He, G., Xu, X., Li, H., Sun, G., Yang, T., Gao, L., Zhu, Z., 2006. Crustal tectonic framework of northern Xinjiang and adjacent regions and its formation. Acta Geol. Sin. 80, 148–168 (in Chinese with English abstract).

Li, Q., Lü, S., Yang, F., Geng, X., Chai, F., 2015. Geological characteristics and genesis of the Laoshankou Fe-Cu-Au deposit in Junggar, Xinjiang, Central Asian Orogenic Belt. Ore Geol. Rev. 68, 57–78.

Li, Q., Zhang, Z., Geng, X., Li, C., Liu, F., Chai, F., Yang, F., 2014. Geology and geochemistry of the Qiaoxiahala Fe–Cu–Au deposit, Junggar region, northwest China. Ore Geol. Rev. 57, 462–481.

Li, X., Qi, C., Liu, Y., Liang, X., Tu, X., Xie, L., Yang, Y., 2005. Petrogenesis of the Neoproterozoic bimodal volcanic rocks along the western margin of the Yangtze Block: new constraints from Hf isotopes and Fe/Mn ratios. Chin. Sci. Bull. 50, 2481–2486.

Li, X.H., Long, W.G., Guo, C.H., Liu, Y., Li, Q.L., Hu, Z.C., Tao, H., 2008. Penglai zircon: a potential new reference for microbeam analysis of U-Pb age and O-Hf isotopes. Geochim. Cosmochim. Acta 72.

Li, Z., Han, B., Song, B., 2004. SHRIMP zircon U-Pb dating of the Ertaibei granodiorite and its enclaves from eastern Junggar, Xinjiang, and geological implications. Acta Petrol. Sin. 20, 1263–1270 (in Chinese with English abstract).

Liang, P., Chen, H., Hollings, P., Wu, C., Xiao, B., Bao, Z., Xu D., submitted for publication. Geochronology and geochemistry of igneous rocks from the laoshankou district, north xinjiang: implications for the late paleozoic tectonic evolution and metallogenesis of east junggar.

Liang, X., Wei, G., Li, X., Liu, Y., 2003. Precise measurement of $^{143}Nd/^{144}Nd$ and Sm/Nd ratios using multiple-collectors inductively coupled plasma-mass spectrometer (MC-ICPMS). Geochimica 32, 91–96 (in Chinese with English abstract).

Liégeois, J.P., 1998. Some words on the post-collisional magmatism. Lithos 45, 15–18.

Liu, Y., Gao, S., Hu, Z., Gao, C., Zong, K., Wang, D., 2010. Continental and oceanic crust recycling-induced melt-peridotite interactions in the Trans-North China Orogen: U-Pb dating, Hf isotopes and trace elements in zircons from mantle xenoliths. J. Petrol. 51, 537–571.

Long, L., Wang, J., Wang, Y., Wang, L., Wang, S., Pu, K., 2009. Geochronology and geochemistry of the ore-bearing porphyry in Xilekuduke Cu-Mo deposit, Fuyun area, Xinjiang, China. Geol. Bull. China 28, 1840–1851 (in Chinese with English abstract).

Long, L., Wang, Y., Du, A., Wang, J., Wang, L., Wang, S., Pu, K., Qu, W., 2011. Molybdenite Re-Os age of Xilekuduke Cu-Mo deposit in Xinjiang and its geological significance. Miner. Depos. 30, 635–644 (in Chinese with English abstract).

Long, L., Wang, Y., Wang, J., Wang, L., Li, Q., Wang, S., Pu, K., Zhang, H., Liao, Z., 2010. Magma mixing in the Xilekuduke Cu-Mo ore district in Xinjiang: evidence from zircon U-Pb chronology. Acta Geol. Sin. 26, 449–456 (in Chinese with English abstract).

Long, X., Yuan, C., Sun, M., Safonova, I., Xiao, W., Wang, Y., 2012. Geochemistry and U-Pb detrital zircon dating of Paleozoic graywackes in East Junggar, NW China: insights into subduction–accretion processes in the southern Central Asian Orogenic Belt. Gondwana Res. 21, 637–653.

Long, X., Yuan, C., Sun, M., Xiao, W., Zhao, G., Wang, Y., Cai, K., Xia, X., Xie, L., 2010. Detrital zircon ages and Hf isotopes of the early Paleozoic flysch sequence in the Chinese Altai, NW China: new constrains on depositional age, provenance and tectonic evolution. Tectonophysics 480, 213–231.

Lu, S., 2012. Metallogenic Mechanism of Laoshankou Fe-Cu-Au Deposit in Qinghe Country, Xinjiang Master's Thesis. China University of Geosciences, Beijing, pp. 1–96 (in Chinese with English abstract).

Lu, S., Yang, F., Chai, F., Geng, X., 2013. Geochemical features of granitoids in Laoshankou Ore district on northern margin of East Junggar, Xinjiang. Geol. Rev. 59, 971–982 (in Chinese with English abstract).

Lu, S., Yang, F., Chai, F., Zhang, X., Jiang, L., Liu, F., Zhang, Z., Geng, X., Ouyang, L., 2012. Zircon U-Pb dating for intrusions in Laoshankou ore district in northern margin of East Junggar and their significances. Geol. Rev. 58, 149–164 (in Chinese with English abstract).

Ludwig, K.R., 2003. User's Manual for Isoplot 3.00: A Geochronological Toolkit for Microsoft Excel. Kenneth R. Ludwig.

Maniar, P.D., Piccoli, P.M., 1989. Tectonic discrimination of granitoids. Geol. Soc. Am. Bull. 101, 635–643.

McKenzie, D., O'nions, R., 1991. Partial melt distributions from inversion of rare earth element concentrations. J. Petrol. 32, 1021–1091.

Middlemost, E.A., 1994. Naming materials in the magma/igneous rock system. Earth Sci. Rev. 37, 215–224.

Münker, C., Wörner, G., Yogodzinski, G., Churikova, T., 2004. Behaviour of high field strength elements in subduction zones: constraints from Kamchatka-Aleutian arc lavas. Earth Planet. Sci. Lett. 224, 275–293.

Niu, H.C., Yu, X., Xu, J., 2006. The Neopaleozoic Volcanism and Mineralization in Altay. Geological Publishing House, Beijing, China (in Chinese with English abstract).
Olafsson, M., Eggler, D.H., 1983. Phase relations of amphibole, amphibole-carbonate, and phlogopite-carbonate peridotite: petrologic constraints on the asthenosphere. Earth Planet. Sci. Lett. 64, 305–315.
Pang, X., Wang, Y., Wei, W., Xu, B., 2009. Sedimentary facies of the Lower Carboniferous Nanmingshui Formation in Fuyun County, Xinjiang and their palaeogeography signification. Acta Petrol. Sin. 25, 682–688 (in Chinese with English abstract).
Pearce, J., Peate, D., 1995. Tectonic implications of the composition of volcanic arc magmas. Annu. Rev. Earth Planet. Sci. 23, 251–286.
Pearce, J.A., 1982. Trace element characteristics of lavas from destructive plate boundaries. Andesites, 525–548.
Pearce, J.A., Norry, M.J., 1979. Petrogenetic implications of Ti, Zr, Y, and Nb variations in volcanic rocks. Contrib. Miner. Petrol. 69, 33–47.
Pirajno, F., Mao, J., Zhang, Z., Zhang, Z., Chai, F., 2008. The association of mafic–ultramafic intrusions and A-type magmatism in the Tian Shan and Altay orogens, NW China: implications for geodynamic evolution and potential for the discovery of new ore deposits. J. Asian Earth Sci. 32, 165–183.
Pitcher, W.S., 1997. The Nature and Origin of Granite. Springer Science & Business Media.
Plank, T., Langmuir, C.H., 1998. The chemical composition of subducting sediment and its consequences for the crust and mantle. Chem. Geol. 145, 325–394.
Qi, L., Hu, J., Conrad, D.G., 2000. Determination of trace elements in granites by inductively coupled plasma mass spectrometry. Talanta 51, 507–513.
Rapp, R.P., Watson, E.B., 1995. Dehydration melting of metabasalt at 8–32 kbar: implications for continental growth and crust-mantle recycling. J. Petrol. 36, 891–931.
Robinson, J.A.C., Wood, B.J., 1998. The depth of the spinel to garnet transition at the peridotite solidus. Earth Planet. Sci. Lett. 164, 277–284.
Rudnick, R., Gao, S., 2003. Composition of the continental crust. Treatise Geochem. 3, 1–64.
Scherer, E., Münker, C., Mezger, K., 2001. Calibration of the lutetium-hafnium clock. Science 293, 683–687.
Schiano, P., Clocchiatti, R., Shimizu, N., Maury, R., Jochum, K., Hofmann, A., 1995. Hydrous, silica-rich melts in the sub-arc mantle and their relationship with erupted arc lavas. Nature 377, 595–600.
Segal, I., Halicz, L., Platzner, I.T., 2003. Accurate isotope ratio measurements of ytterbium by multiple collection inductively coupled plasma mass spectrometry applying erbium and hafnium in an improved double external normalization procedure. J. Anal. At. Spectrom. 18, 1217–1223.
Sengor, A.M.C., Natalin, B.A., Burtman, V.S., 1993. Evolution of the Altaid tectonic collage and Paleozoic crustal growth in Eurasia. Nature 364, 299–307.
Shen, X., Zhang, H., Wang, Q., Wyman, D.A., Yang, Y., 2011. Late Devonian-Early Permian A-type granites in the southern Altay Range, Northwest China: petrogenesis and implications for tectonic setting of "A2-type" granites. J. Asian Earth Sci. 42, 986–1007.
Song, G., Qin, K., Liu, T., Li, G., Shen, P., 2010. The U-Pb ages, Hf isotope and REE patterns of older zircons from Devonian volcanic rocks in Ashele basin on the southern margin of Altai orogen and its geological significance. Acta Petrol. Sin. 26, 2946–2958 (in Chinese with English abstract).
Sun, M., Yuan, C., Xiao, W., Long, X., Xia, X., Zhao, G., Lin, S., Wu, F., Kroener, A., 2008. Zircon U-Pb and Hf isotopic study of gneissic rocks from the Chinese Altai: progressive accretionary history in the early to middle Palaeozoic. Chem. Geol. 247, 352–383.
Sun, S.S., McDonough, W.F., 1989. Chemical and isotopic systematics of oceanic basalts: implications for mantle composition and processes. Geol. Soc. Lond. Spec. Publ. 42, 313–345.
Tang, H., Chen, Y., Liu, Y., Huang, B., 2006. Isotope dating of the Be'erkuduke tin deposit in the eastern Junggar area. J. Miner. Petrol. 26, 71–73 (in Chinese with English abstract).
Taylor, S.R., McLennan, S.M., 1985. The Continental Crust: Its Composition and Evolution.
Thirlwall, M., Smith, T., Graham, A., Theodorou, N., Hollings, P., Davidson, J., Arculus, R., 1994. High field strength element anomalies in arc lavas: source or process? J. Petrol. 35, 819–838.
Thompson, M., Potts, P.J., Kane, J.S., Wilson, S., 1999. GEOPT5—an international proficiency test for analytical geochemistry laboratories. Rep. Round 5, 23.
Tong, Y., Wang, T., Kovach, V., Hong, D., Han, B., 2006. Age and origin of the Takeshiken postorogenic alkali-rich intrusive rocks in southern Altai, near the Mongolian border in China and its implications for continental growth. Acta Petrol. Sin. 22, 1267–1278 (in Chinese with English abstract).
Tong, Y., Wang, T., Siebel, W., Hong, D.W., Sun, M., 2012. Recognition of early Carboniferous alkaline granite in the southern Altai orogen: post-orogenic processes constrained by U-Pb zircon ages, Nd isotopes, and geochemical data. Int. J. Earth Sci. 101, 937–950.
Turner, S., Foden, J., Morrison, R., 1992. Derivation of some A-type magmas by fractionation of basaltic magma: an example from the Padthaway Ridge, South Australia. Lithos 28, 151–179.
Wan, B., Xiao, W., Han, C., Windley, B.F., Zhang, L., Qu, W., Du, A., 2014. Re–Os molybdenite age of the Cu–Mo skarn ore deposit at Suoerkuduke in East Junggar, NW China and its geological significance. Ore Geol. Rev. 56, 541–548.
Wan, B., Xiao, W., Zhang, L., Windley, B.F., Han, C., Quinn, C.D., 2011. Contrasting styles of mineralization in the Chinese Altai and East Junggar, NW China: implications for the accretionary history of the southern Altaids. J. Geol. Soc. 168, 1311–1321.
Wan, B., Zhang, L., 2006. Sr-Nd-Pb isotope geochemistry and tectonic setting of Devonian polymetallic metallogenic belt on the Southern margin of Altaid, Xingjing. Acta Petrol. Sin. 22, 145–152 (in Chinese with English abstract).
Wang, J., Xu, X., 2006. Post-collisional tectonic evolution and metallogenesis in northern Xinjiang, China. Acta Geol. Sin. 80, 23–31 (in Chinese with English abstract).
Wang, Q., Wyman, D.A., Li, Z.X., Bao, Z.W., Zhao, Z.H., Wang, Y.X., Jian, P., Yang, Y. H., Chen, L.L., 2010. Petrology, geochronology and geochemistry of ca. 780 Ma A-type granites in South China: petrogenesis and implications for crustal growth during the breakup of the supercontinent Rodinia. Precambr. Res. 178, 185–208.
Wang, T., Tong, Y., Li, S., Zhang, J., Shi, X., Li, J., Han, B.F., Hong, D., 2010. Spatial and temporal variations of granitoids in the Altay orogen and their implications for tectonic setting and crustal growth: perspectives from Chinese Altay. Acta Petrol. Mineral. 29, 595–618 (in Chinese with English abstract).
Wang, T., Jahn, B.M., Kovach, V.P., Tong, Y., Hong, D.W., Han, B.F., 2009. Nd–Sr isotopic mapping of the Chinese Altai and implications for continental growth in the Central Asian Orogenic Belt. Lithos 110, 359–372.
Wang, T., Hong, D.W., Jahn, B.M., Tong, Y., Wang, Y.B., Han, B.F., Wang, X.X., 2006. Timing, petrogenesis, and setting of Paleozoic synorogenic intrusions from the Altai Mountains, northwest China: implications for the tectonic evolution of an accretionary orogen. J. Geol. 114, 735–751.
Wei, G.J., Liang, X., Li, X., Liu, Y., 2002. Precise measurement of Sr isotopic composition of liquid and solid base using (LP) MC-ICPMS. Geochimica 31, 295–305 (in Chinese with English abstract).
Wei, G., Ni, Z., 1990. Preliminary study of the rift volcanic rocks of the Irtysh volcanic area, Xinjiang. J. Mineral. Petrol. 10, 15–23 (in Chinese with English abstract).
Whalen, J.B., Currie, K.L., Chappell, B.W., 1987. A-type granites: geochemical characteristics, discrimination and petrogenesis. Contrib. Miner. Petrol. 95, 407–419.
White, W., Hofmann, A., 1982. Sr and Nd isotope geochemistry of oceanic basalts and mantle evolution. Nature 298, 821–825.
Winchester, J., Floyd, P., 1977. Geochemical discrimination of different magma series and their differentiation products using immobile elements. Chem. Geol. 20, 325–343.
Wilson, B.M., 1989. Igneous Petrogenesis a Global Tectonic Approach. Springer.
Windley, B.F., Alexeiev, D., Xiao, W., Kröner, A., Badarch, G., 2007. Tectonic models for accretion of the Central Asian Orogenic Belt. J. Geol. Soc. 164, 31–47.
Windley, B.F., Kroner, A., Guo, J.H., Qu, G.S., Li, Y.Y., Zhang, C., 2002. Neoproterozoic to Paleozoic geology of the Altai orogen, NW China: new zircon age data and tectonic evolution. J. Geol. 110, 719–737.
Wood, D.A., 1980. The application of a Th-Hf-Ta diagram to problems of tectonomagmatic classification and to establishing the nature of crustal contamination of basaltic lavas of the British Tertiary Volcanic Province. Earth Planet. Sci. Lett. 50, 11–30.
Wright, J., 1969. A simple alkalinity ratio and its application to questions of non-orogenic granite genesis. Geol. Mag. 106, 370–384.
Wu, C., Chen, H., Hollings, P., Xu, D., Liang, P., Han, J., Xiao, B., Cai, K., Liu, Z., Qi, Y., 2015. Magmatic sequences in the Halasu Cu belt, NW China: trigger for the Paleozoic porphyry Cu mineralization in the Chinese Altay-East Junggar. Ore Geol. Rev. 71, 373–404.
Wu, G.G., Dong, L.H., Xue, C.J., 2008. Main Porphyry Copper Ore Belt in Northern Xinjiang. Geological Publishing House, China, Beijing (in Chinese).
Wu, S.P., Wang, M.Y., QI, K.J., 2007. Present situation of researches on A-type granites: a review. Acta Petrol. Mineral. 26, 57–66 (in Chinese with English abstract).
Wyman, D., Ayer, J., Devaney, J., 2000. Niobium-enriched basalts from the Wabigoon subprovince, Canada: evidence for adakitic metasomatism above an Archean subduction zone. Earth Planet. Sci. Lett. 179, 21–30.
Xiang, P., Zhang, L.C., Wu, H.Y., Zhang, X.J., Chen, Z.G., Wan, B., 2009. Ages of the zircons from ore-bearing porphyries in II-III ore area of Kalaxianger porphyry copper ore belt in Qinghe, Xinjiang and its geological significance. Acta Petrol. Sin. 25, 1474–1483 (in Chinese with English abstract).
Xiao, W.J., Han, C., Yuan, C., Sun, M., Lin, S., Chen, H., Li, Z., Li, J., Sun, S., 2008. Middle Cambrian to Permian subduction-related accretionary orogenesis of Northern Xinjiang, NW China: implications for the tectonic evolution of central Asia. J. Asian Earth Sci. 32, 102–117.
Xiao, W.J., Windley, B., Badarch, G., Sun, S., Li, J., Qin, K., Wang, Z., 2004. Palaeozoic accretionary and convergent tectonics of the southern Altaids: implications for the growth of Central Asia. J. Geol. Soc. 161, 339–342.
Xiao, W.J., Windley, B.F., Huang, B.C., Han, C.M., Yuan, C., Chen, H.L., Sun, M., Sun, S., Li, J.L., 2009. End-Permian to mid-Triassic termination of the accretionary processes of the southern Altaids: implications for the geodynamic evolution, Phanerozoic continental growth, and metallogeny of Central Asia. Int. J. Earth Sci. 98, 1189–1217.
Xie, L., Wang, R., Wang, D., Qiu, J., 2005. Contrasting accessory mineral assemblages in the Taohuadao peralkaline and Putuoshan aluminous A-type granites, Zhejiang Province. Geol. J. China Univ. 11, 390–403 (in Chinese with English abstract).
Xu, J., Mei, H., Yu, X., Bai, Z., Niu, H., Chen, F., Zhen, Z., Wang, Q., 2001. Adakites related to subduction in the northern margin of Junggar arc for the Late Paleozoic: products of slab melting. Chin. Sci. Bull. 46, 1312–1316.

Xu, X.W., Jiang, N., Li, X.H., Qu, X., Yang, Y.H., Mao, Q., Wu, Q., Zhang, Y., Dong, L.H., 2013. Tectonic evolution of the East Junggar terrane: evidence from the Taheir tectonic window, Xinjiang, China. Gondwana Res. 24, 578–600.

Xu, Y.G., Menzies, M.A., Thirlwall, M.F., Xie, G.H., 2001. Exotic lithosphere mantle beneath the western Yangtze craton: petrogenetic links to Tibet using highly magnesian ultrapotassic rocks. Geology 29, 863–866.

Xue, C., Zhao, Z., Wu, G., Dong, L., Feng, J., Zhang, Z., Zhou, G., Chi, G., Gao, J., 2010. The multiperiodic superimposed porphyry copper mineralization in Central Asian Tectonic Region: a case study of geology, geochemistry and chronology of Halasu copper deposit, Southeastern Altai, China. Earth Sci. Front. 17, 53–82 (in Chinese with English abstract).

Yakubchuk, A., 2004. Architecture and mineral deposit settings of the Altaid orogenic collage: a revised model. J. Asian Earth Sci. 23, 761–779.

Yan, S.H., Teng, R.L., Zhang, Z.C., Chen, B.L., Chen, W., Zhou, G., He, L.X., 2006. New understanding on origin of Kalaxiangeer copper deposit on southern margin of Altay mountain, Xinjiang: constraints from S-Pb-H-O isotope geochemistry and ^{40}Ar-^{39}Ar age of Halasu copper deposit. Miner. Depos. 25, 292–301 (in Chinese with English abstract).

Yan, S., Zhang, Z., Wang, Y., Chen, B., Zhou, G., He, L., 2005. REE geochemistry of Qiaoxiahala type Fe-Cu deposits in southern margin of Altay Mountains, Xinjiang, and its geological implications. Miner. Depos. 24, 25–33 (in Chinese with English abstract).

Yang, F., Chai, F., Zhang, Z., Geng, X., Li, Q., 2014. Zircon U-Pb geochronology, geochemistry and Sr–Nd–Hf isotopes of granitoids in the Yulekenhalasu copper ore district, northern Junggar, China: petrogenesis and tectonic implications. Lithos 190–191, 85–103.

Yang, F., Yan, S., Qu, W., Zhou, G., Liu, F., Geng, X., Liu, G., Wang, X., 2010. The fluid inclusions and C, H and O isotopic geochemistry of the I mineralized zone at the Halasu copper deposit, Xinjiang. Earth Sci. Front. 17, 359–374 (in Chinese with English abstract).

Yang, F.Q., Zhang, Z.X., Liu, G.R., Qu, W.J., Zhang, L.W., Wei, G.Z., Liu, F., Chai, F.M., 2012. Geochronology of Yulekenhalasu porphyry copper deposit in northern Junggar area, Xinjiang, China. Acta Petrol. Sin. 28, 2029–2042 (in Chinese with English abstract).

Yao, H., Zhao, H., Xue, H., 2007. Geochemical characteristics of the ore-bearing porphyry in Kalasayi porphyry Cu deposit, Qinghe, Xinjiang. Xinjiang Nonferr. Metals 30, 7–8 (in Chinese).

Ying, L., 2007. Geology, geochemistry and discussion on the origin of the Qiaoxiahala Fe-Cu-Au deposit in Xinjiang Master's Thesis. Chinese Academy of Geological Sciences, Beijing, pp. 1–112 (in Chinese with English abstract).

Zartman, R., Doe, B., 1981. Plumbotectonics—the model. Tectonophysics 75, 135–162.

Zhang, Z., Chai, F., Du, A., Zhang, Z., Yan, S., Yang, J., Qu, W., Wang, Z., 2005. Re–Os dating and ore-forming material tracing of the Karatungk Cu–Ni sulfide deposit in northern Xinjiang. Acta Petrol. Mineral. 24, 285–293.

Zhang, Z., Yang, F., Li, C., Liu, F., Geng, X., Liu, G., Chai, F., Ouyang, L., 2012. Rock-forming and ore-forming ages of Qiaoxiahala Fe-Cu-Au deposit on northern margin of Junggar Basin, Xinjiang. Miner. Depos. 31, 347–358 (in Chinese with English abstract).

Zhang, Z., Zhou, G., Kusky, T.M., Yan, S., Chen, B., Zhao, L., 2009. Late Paleozoic volcanic record of the Eastern Junggar terrane, Xinjiang, Northwestern China: major and trace element characteristics, Sr–Nd isotopic systematics and implications for tectonic evolution. Gondwana Res. 16, 201–215.

Zhang, Z.C., Yan, S.H., Chen, B., Zhou, G., He, Y.K., Chai, F.M., He, L.X., Wan, Y.S., 2006. SHRIMP U-Pb zircon age of subduction granite in the north of East Junggar, Xinjiang. Chin. Sci. Bull. 51, 1565–1574 (in Chinese).

Zhao, L., Wang, J., Wang, Y., Wang, L., Ding, R., Long, L., Li, D.D., 2015. Zircon SHRIMP geochronology of Suoerkuduke Cu-Mo deposit in Xinjiang, and its geological significance. Acta Petrol. Sin. 31, 435–448 (in Chinese with English abstract).

Zhao, Z., Xue, C., Zhang, L., Wen, C., Zhou, G., Liu, G., 2009. U-Pb dating of zircons from acid intrusions in Yulekenhalasu copper deposit of Qinghe, Xinjiang, and its geological significance. Miner. Depos. 28, 425–433 (in Chinese with English abstract).

Zhou, G., Wu, G., Dong, L., Zhang, Z., Dong, Y., Tong, Y., He, L., Ying, L., 2009. Formation time and geochemical feature of Wutubulak pluton in the northeastern margin of Junggar in Xinjiang and its geological significance. Acta Petrol. Sin. 25, 1390–1402 (in Chinese with English abstract).

Zhou, G., Zhang, Z., Gu, G., Yang, W., He, B., Zhang, X., Luo, S., Wang, X., He, Y., 2006. Dating of granitic plutons and its geological implications in the lower reaches of the Qinggeli River in the northern part of East Junggar, Xinjiang. Geosciences 20, 141–150 (in Chinese with English abstract).

Zindler, A., Hart, S., 1986. Chemical geodynamics. Annu. Rev. Earth Planet. Sci. 14, 493–571.